

Electronic excitation spectra of the Emery model

P. Unger and P. Fulde

Max-Planck-Institut für Festkörperforschung, D-7000 Stuttgart 80, Germany

(Received 24 August 1992)

We calculate the photoemission and inverse photoemission spectra of holes in copper-oxygen planes, the characteristic structural unit of high-temperature superconductors. The computations are based on the extended Hubbard or Emery model in the limit of infinitely strong Coulomb repulsion U_d on copper sites. In order to evaluate the corresponding one-particle correlation functions the projection technique is applied, which is especially suitable for strongly correlated systems. Thereby the hole dynamics is restricted to a subspace of relevant operators, within which it can be treated exactly. In contrast to independent-particle approximations the excitation spectra show an energy gap at half-filling, which disappears when the system is doped with additional holes. Besides the insulator-to-metal transition the strong correlations lead also to a significant shift of spectral weight to states close to the Fermi energy when the hole concentration increases. Our results are in good agreement with the ones of exact diagonalization studies of the $(\text{CuO}_2)_4$ cluster with periodic boundary conditions.

I. INTRODUCTION

It is well known that the copper oxide-based high-temperature superconducting materials are systems in which electron correlation are strong. This is demonstrated by the experimental observation that, e.g., La_2CuO_4 is a semiconductor and not a metal although there is one hole per unit cell, suggesting a half-filled conduction band. The reason for the strong correlation is easily found. Consider the all important copper-oxygen planes of these materials. The Coulomb repulsion between two d holes on a copper site is found from constraint local-density-approximation (LDA) calculations to be of order $U_d = 10.5$ eV, while the hopping matrix element of a hole from a Cu $3d_{x^2-y^2}$ orbital to an O $2p_{x(y)}$ orbital is $t_{pd} = 1.3$ eV. It is the large value of U_d as compared with the bandwidth which is responsible for the strong electron correlations and that the system is an insulator instead of a metal.

A computation of dynamical correlation functions for holes in the planes should therefore start out from an accurate treatment of U_d while the effect of $t_{pd} \ll U_d$ can be dealt with in an approximate manner. This is contrary to conventional theories of interacting electrons, where it is the interaction which is treated approximately only, e.g., by using Feynman diagrams.

Recently a theory was developed^{1,2} which can be applied to weakly and strongly correlated electrons. It does not make use of Feynman diagrams, which require Wick's theorem and are especially useful when electron interactions are relatively weak (i.e., when $t_{pd} \gg U_d$). Instead, the computation of dynamical correlation functions is based on projection techniques. The former are expressed in terms of cumulants which eliminate statistically independent processes (i.e., unlinked clusters in case of diagrams) from the calculation.

The aim of this investigation is to calculate the photoemission and inverse photoemission spectra for the

copper-oxygen planes at half-filling and when the system is doped, i.e., when the hole concentration $n_h > 1$ deviates from half-filling. This is done within the framework of the Emery model Hamiltonian of Ref. 3 (Sec. II), where for simplicity the Coulomb interaction of holes at copper sites is assumed to be infinitely strong. The same problem was investigated previously by numerical diagonalization of a $(\text{CuO}_2)_4$ cluster and applying periodic boundary conditions.^{4,5} Thereby it was found that the spectra show a number of properties, in particular when changes due to hole doping are considered, which cannot be explained by conventional band theory and are solely due to the strong correlations. Our aim here is to study these features by analytic methods, i.e., by application of projection techniques. This can be done by using a relatively small number of dynamical variables only. The present investigation extends previous work on the photoelectron spectrum for half-filling.⁶

The paper is organized as follows. The projection method is briefly reviewed in Sec. III. The following sections describe the approximation within which the ground state is treated from which an electron is ejected (photoemission) or to which it is added (inverse photoemission) as well as the computation of the spectra. Section VII contains the discussion of the results while a brief summary is given in Sec. VIII.

II. EMERY MODEL

Our investigation of electronic excitations in high-temperature superconductors is based on the extended Hubbard or Emery model. The Hamiltonian describes charge carriers of the copper-oxide plane and is formulated in the hole picture. Two different types of localized states are considered, namely, O $2p_{x(y)}$ and Cu $3d_{x^2-y^2}$

orbitals, connected by hopping matrix elements between nearest neighbors and nearest oxygen sites. As mentioned before, the dominant correlation between holes in high-temperature superconductors is their Coulomb repulsion on copper sites. We restrict ourselves to the limit of infinitely strong interaction by simply excluding doubly occupied Cu 3d states. Thus, the 3d⁸ configuration is completely suppressed. With respect to the excitation spectra the Coulomb repulsion within oxygen orbitals U_p is of minor importance since for low levels of doping the hole occupation number of oxygen sites is rather small. This point has been confirmed by exact diagonalization studies.⁷ Therefore, we may ignore the influence of two-particle interactions within the oxygen system. Under those restrictions the Hamiltonian of the Emery model may be written in the form

$$\begin{aligned}
 H &= H'_0 + H'_1, \\
 H'_0 &= e_p \sum_{iI\sigma} p_{iI\sigma}^\dagger p_{iI\sigma} + \sum_{IJ} \sum_{ij\sigma} T_{ij}^{pp} p_{iI\sigma}^\dagger p_{jJ\sigma} \\
 &\quad + e_d \sum_{\alpha I\sigma} \hat{d}_{\alpha I\sigma}^\dagger \hat{d}_{\alpha I\sigma}, \\
 H'_1 &= \sum_{IJ} \sum_{i\alpha\sigma} T_{i\alpha}^{pd} \left(p_{iI\sigma}^\dagger \hat{d}_{\alpha J\sigma} + \hat{d}_{\alpha J\sigma}^\dagger p_{iI\sigma} \right).
 \end{aligned} \tag{1}$$

The $p_{iI\sigma}^\dagger$ operator creates a hole in an O 2p orbital in unit cell I with site index i and spin σ . In contrast to $p_{iI\sigma}^\dagger$ the Hubbard operators $\hat{d}_{\alpha I\sigma}^\dagger$ do not fulfill fermionic anticommutation relations since they act under the restriction that no doubly occupied copper sites be generated. They are related to the fermionic creation operator for Cu 3d orbitals $d_{\alpha I\sigma}^\dagger$ through $\hat{d}_{\alpha I\sigma}^\dagger = d_{\alpha I\sigma}^\dagger (1 - d_{\alpha I-\sigma}^\dagger d_{\alpha I-\sigma})$. The hopping matrix elements T_{ij}^{pp} and $T_{\alpha j}^{pd}$ connect neighboring O-O and Cu-O orbitals, respectively. The signs of the different matrix elements are determined by the symmetry properties of the underlying p - and d -wave functions:

$$T_{ij}^{pp} = -\varphi_i \varphi_j t_{pp}, \quad T_{i\alpha}^{pd} = -\varphi_i \varphi_\alpha t_{pd}. \tag{2}$$

Thereby the phase factors $\varphi_1 = \varphi_2 = \varphi_A = -1$ and $\varphi_3 = \varphi_4 = \varphi_B = 1$ have been used. The indices $i, j = 1, \dots, 4$ and $\alpha = A, B$ refer to the oxygen and copper orbitals of the antiferromagnetic unit cell in Fig. 1. A reasonable parameter set for high-temperature superconductors can be extracted from band-structure calculations by mapping their results to the Emery model. Hybertsen, Schlüter, and Christensen⁸ give the values $\Delta = e_p - e_d = 3.6$ eV, $t_{pd} = 1.3$ eV, and $t_{pp} = 0.65$ eV.

The Coulomb repulsion of holes on copper sites is the dominant term in the Hamiltonian of Eq. (1) causing strong correlations between the charge carriers. To yield reasonable results the exclusion of double occupancy has to be respected rigorously. Therefore the two-particle interaction cannot be treated as a small perturbation but should be included right from the beginning in the unperturbed part H'_0 of the Hamiltonian H . The copper and oxygen states, which are independent from each other in H'_0 , are then coupled by nearest-neighbor hopping processes $T_{i\alpha}^{pd}$ in the perturbation H'_1 .

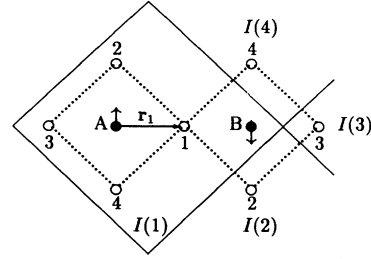


FIG. 1. Unit cell of the copper-oxygen plane: four oxygen orbitals (circles) and two copper orbitals (black dots) form the basis. The spin directions in the Néel-ordered copper system are indicated by small arrows. The four oxygen orbitals of the B plaquette belong to the unit cells $I(1), \dots, I(4)$.

For later reference we introduce the operators $p_{i\mathbf{k}\sigma}^\dagger$ and $\hat{d}_{\alpha\mathbf{k}\sigma}^\dagger$ which create holes with momentum \mathbf{k} and spin σ :

$$p_{i\mathbf{k}\sigma}^\dagger = \frac{1}{\sqrt{N}} \sum_I e^{-i\mathbf{k} \cdot \mathbf{R}_{Ii}} p_{iI\sigma}^\dagger, \tag{3}$$

$$\hat{d}_{\alpha\mathbf{k}\sigma}^\dagger = \frac{1}{\sqrt{N}} \sum_I e^{-i\mathbf{k} \cdot \mathbf{R}_{I\alpha}} \hat{d}_{\alpha I\sigma}^\dagger. \tag{4}$$

Here, $\mathbf{R}_{Ii} = \mathbf{R}_I + \mathbf{r}_i$ (or $\mathbf{R}_{I\alpha}$) is a vector pointing to the orbital i (or α , respectively) in cell I . As an example, the vector \mathbf{r}_1 is shown in Fig. 1. If we consider exclusively the four oxygen orbitals on an A plaquette in cell I there is only one linear combination $p_{AI\sigma}^\dagger$ which is coupling via T_{iA}^{pd} to the central copper site:

$$p_{AI\sigma}^\dagger = \frac{1}{2} (p_{1I\sigma}^\dagger + p_{2I\sigma}^\dagger - p_{3I\sigma}^\dagger - p_{4I\sigma}^\dagger). \tag{5}$$

This linear combination is called the symmetric one since it has the same symmetry as the hopping matrix element $T_{i\alpha}^{pd}$. The corresponding creation operator $p_{BI\sigma}^\dagger$ with respect to the B plaquette in cell I is given by

$$p_{BI\sigma}^\dagger = \frac{1}{2} (p_{1I(1)\sigma}^\dagger + p_{2I(2)\sigma}^\dagger - p_{3I(3)\sigma}^\dagger - p_{4I(4)\sigma}^\dagger). \tag{6}$$

The cell indices $I(1), \dots, I(4)$ are depicted in Fig. 1. We distinguish the symmetric creation operators $p_{i\alpha I\sigma}^\dagger$ from the oxygen operators of site i , $p_{iI\sigma}^\dagger$, by a Greek instead of an italic index. In the following, the index α always replaces A, B , whereas i or j stands for $1, \dots, 4$. According to Eq. (3) we define the operator $p_{\alpha\mathbf{k}\sigma}^\dagger$ by

$$p_{\alpha\mathbf{k}\sigma}^\dagger = \frac{1}{\sqrt{N}} \sum_I e^{-i\mathbf{k} \cdot \mathbf{R}_{I\alpha}} p_{iI\sigma}^\dagger. \tag{7}$$

The spectra for addition or removal of oxygen or copper holes are obtained from the corresponding dynamical correlation functions. The latter are of the form

$$G(t) = \langle \Psi | A^\dagger e^{-it(H-E_o)} A | \Psi \rangle, \tag{8}$$

where A stands for $p_{iI\sigma}^\dagger$, $p_{iI\sigma}$, $\hat{d}_{\alpha I\sigma}^\dagger$, or $\hat{d}_{\alpha I\sigma}$. Here, E_o denotes the energy of the exact ground state $|\Psi\rangle$ of the Hamiltonian H . The resulting spectral densities can

be compared with measurements of photoemission and inverse photoemission spectra of doped copper-oxygen planes.

III. PROJECTION TECHNIQUE

The starting point of the usual many-particle perturbation theory is an unperturbed system of free fermions or bosons. The one-particle Green's functions can be calculated using standard diagrammatic techniques. In strongly correlated systems, Wick's theorem no longer holds (at least in its conventional form) since the unperturbed Hamiltonian contains the interaction terms and the creation and annihilation operators do not fulfill fermionic or bosonic commutation relations. Therefore, we apply a different approach to the evaluation of dynamical correlation functions being especially suitable for strongly correlated systems. In this formalism, there is no restriction with respect to the form of the unperturbed Hamiltonian H_0 .

As in the standard diagrammatic technique the time evolution operator $U(t) = \exp(-itH)$ is divided into an unperturbed and a perturbed part. Usually a time dependent operator $H_1(t) = \exp(itH_0)H_1 \exp(-itH_0)$ and a time-ordered exponential \exp_T are introduced, which leads to the representation

$$U(t) = \exp(-itH_0) \exp_T \left(-i \int_0^t dt' H_1(t') \right). \quad (9)$$

Instead, we apply the decomposition

$$U(t) = \exp[-it(H_1 + \mathcal{L}_o)] \exp(-itH_0). \quad (10)$$

The Liouville operator \mathcal{L}_o is a superoperator acting on normal operators X according to the definition

$$\mathcal{L}_o X = [H_0, X]_-. \quad (11)$$

With the help of Eq. (10) the dynamical correlation function of Eq. (8) can be transformed into an expectation value with respect to the ground state of H_0 symbolized by the bracket $|\cdot\rangle$. The details of the derivation are described in Ref. 2. The Laplace transform of $G(t)$ takes then the form

$$G(\omega) = \langle \Omega | A^\dagger \left(\frac{1}{\omega - \mathcal{L}} A \right)^\bullet | \Omega \rangle_c, \quad (12)$$

$$\Omega = 1 + \lim_{x \rightarrow 0} \frac{1}{x - \mathcal{L}_o - H_1} H_1. \quad (13)$$

If expanded in powers of H_1 the operator Ω represents the usual Rayleigh-Schrödinger perturbation series. It contains the transformation of the unperturbed into the full ground state $|\Psi\rangle$. \mathcal{L} denotes the Liouville operator belonging to H . Most important in Eq. (12) is the index "c" at the right bracket of the expectation value. This abbreviation signals that the cumulant of the operator product with respect to A , \mathcal{L}_o , H_1 , and the expression in large parentheses with black dot $(\dots)^\bullet$ has to be taken. By definition of the cumulant all statistically independent processes, which would contribute to the normal expectation value, drop out of the calculation. Therefore, we

view Eq. (12) as a generalization of Goldstone's linked cluster theorem to strongly correlated systems.

The cumulant $\langle X_1 \cdots X_n \rangle_c$ of an arbitrary operator product is given by the relation⁹

$$\begin{aligned} \langle X_1 \cdots X_n \rangle_c &= \frac{\partial}{\partial \lambda_1} \cdots \frac{\partial}{\partial \lambda_n} \left[\ln \left\langle \prod_{i=1}^n e^{\lambda_i X_i} \right\rangle \right]_{\lambda_1 = \dots = \lambda_n = 0} \end{aligned} \quad (14)$$

Applying this definition one obtains, for example, the following results:

$$\begin{aligned} \langle X_1 \rangle_c &= \langle X_1 \rangle, \\ \langle X_1 X_2 \rangle_c &= \langle X_1 X_2 \rangle - \langle X_1 \rangle \langle X_2 \rangle, \\ \langle X_1 X_2 X_3 \rangle_c &= \langle X_1 X_2 X_3 \rangle - \langle X_1 X_2 \rangle \langle X_3 \rangle - \langle X_1 X_3 \rangle \langle X_2 \rangle \\ &\quad - \langle X_2 X_3 \rangle \langle X_1 \rangle + 2 \langle X_1 \rangle \langle X_2 \rangle \langle X_3 \rangle. \end{aligned}$$

Equation (12) is in a proper form to be evaluated by the Mori-Zwanzig projection technique.^{10,11} In the framework of that formalism, the dynamics of the correlation function $G(\omega)$ is restricted to a relevant subspace of the full operator or Liouville space which is spanned by the operators A_m . Within this subspace, $G(\omega)$ can be calculated exactly. A reasonable choice of the projectors A_m is certainly the most important step in such an approach since the coupling to the remaining part of the Liouville space is neglected. We introduce the projection operator \mathcal{P} being normalized by the inverse of the susceptibility matrix $\underline{\chi}$:

$$\mathcal{P} = \sum_{m,n} | A_m \Omega \rangle_c \chi_{mn}^{-1} \langle \Omega A_n |, \quad (15)$$

$$\chi_{mn} = \langle \Omega | A_m^\dagger A_n | \Omega \rangle_c. \quad (16)$$

In the projection technique, the dynamical correlation function of Eq. (12) is approximated by the expression

$$G(\omega) = \langle \Omega | A^\dagger \left(\mathcal{P} \frac{1}{\omega - \mathcal{P} \mathcal{L} \mathcal{P}} \mathcal{P} A \right)^\bullet | \Omega \rangle_c. \quad (17)$$

After the restriction of the dynamics to a relevant part of the full operator space, $G(\omega)$ can also be expressed in form of a matrix equation containing only the coupling vector \mathbf{c} , the susceptibility matrix $\underline{\chi}$, and the frequency matrix \underline{F} (see, for example, Ref. 12):

$$G(\omega) = \mathbf{c}^\dagger [\omega \cdot \underline{\chi} - \underline{F}]^{-1} \mathbf{c}, \quad (18)$$

$$F_{mn} = \langle \Omega | A_m^\dagger (\mathcal{L} A_n)^\bullet | \Omega \rangle_c, \quad (19)$$

$$c_m = \langle \Omega | A_m^\dagger A | \Omega \rangle_c. \quad (20)$$

One can always find a representation of the projection operators spanning the relevant subspace for which the corresponding frequency and susceptibility matrices both become diagonal. The required similarity transformation is given by the eigenvectors \mathbf{v}_i of the generalized eigenvalue problem

$$\underline{F} \mathbf{v}_i = \epsilon_i \underline{\chi} \mathbf{v}_i. \quad (21)$$

The eigenvectors \mathbf{v}_i , $i = 1, \dots, n$, are normalized with respect to the susceptibility matrix $\underline{\chi}$ according to the

relation $\mathbf{v}_i^\dagger \underline{\chi} \mathbf{v}_j = \delta_{ij}$. For diagonal frequency and susceptibility matrices the inversion of the expression $[\omega \underline{\chi} - \underline{F}]$ in Eq. (18) is a simple task and $G(\omega)$ takes its final form

$$G(\omega) = \sum_{i=1}^n \frac{|\mathbf{c}^\dagger \mathbf{v}_i|^2}{\omega - \epsilon_i}. \quad (22)$$

The corresponding spectral function $S(\omega)$ represents simply a sum over δ functions with pole strengths $|\mathbf{c}^\dagger \mathbf{v}_i|^2$ and pole positions at the eigenvalues ϵ_i .

In conclusion, the program of a projection calculation consists of two steps: First, a reasonable approximation of the full ground state has to be found by expanding Ω in powers of H_1 up to a certain order. Second, the relevant operator space is specified. Afterwards, the spectral function is obtained by diagonalizing the matrices \underline{F} and $\underline{\chi}$. In the next section we describe the ground-state approach in detail. The choice of the projection operators will be discussed separately for the photoemission and inverse photoemission spectra in the subsequent two sections.

IV. GROUND STATE

The unperturbed Hamiltonian H'_0 is easily diagonalized. The eigenvalues form four oxygen bands centered around the orbital energy e_p and include two copper levels at e_d . At half-filling the unperturbed copper system contains one hole per site. Therefore, additional holes created by doping are forced to occupy the lowest oxygen band states. Transitions of holes between the two subsystems arise as soon as the perturbation H'_1 is turned on. Consequently, an expansion of the Ω operator in terms of H'_1 corresponds to a power series in t_{pd}/Δ . We consider that ratio to be the small parameter in the theory. Two types of relevant processes are included in the approximation of the ground state, first an exchange of two neighboring copper spins, which is proportional to t_{pd}^4/Δ^3 and second an exchange of an oxygen and a copper hole within a plaquette proportional to t_{pd}^2/Δ . The resulting Néel order of the copper spins and the modification of the band structure of H'_0 are described in the following.

The ground state of H'_0 is highly degenerate since the spin direction on each copper site is arbitrary. This degeneracy, however, is lifted by the superexchange interaction, which can be described through an antiferromagnetic Heisenberg Hamiltonian H_{se} acting on the copper spins with an exchange constant between nearest neighbors of the form $J = 4t_{pd}^4/\Delta^3$. By adding the Ising part of H_{se} to H'_0 and subtracting it again from H'_1 a Néel ordered copper spin system is obtained as the ground state. We will simply assume this ordering of the copper spins in the following and suppress the additional Hamiltonian H_{se} . For the A sublattice the up spin is chosen and for the B sublattice the down spin (see Fig. 1).

It is well known from experiments that a system like $\text{La}_{2-x}\text{Sr}_x\text{CuO}_4$ is indeed an antiferromagnet for $x = 0$. In addition, the spin dynamics measured by neutron scattering is perfectly consistent with spin-

wave excitations in a two-dimensional, spin- $\frac{1}{2}$ Heisenberg antiferromagnet.¹³ These experimental observations support the assumption of a Néel-ordered copper spin system in the ground state. Although the long-range order disappears with increasing hole concentration, antiferromagnetic correlations between neighboring copper spins are present even at high doping concentrations x . In our approach, the destruction of long-range order by additional charge carriers is ignored since we are interested here in energy scales larger than the one given by the Néel temperature.

As $t_{pd}/\Delta \approx \frac{1}{3}$ an expansion of all matrix elements in \underline{F} and $\underline{\chi}$ up to second order should be a reasonable approximation to determine the excitation spectra correctly on an energy scale of tenths of electron volts. The expansion of the full ground state $|\Omega\rangle_c$ contains in second order the exchange process of oxygen and copper holes mentioned before. Looking at Fig. 2 it becomes clear that this exchange leads to an effective propagation of oxygen holes from one corner of the plaquette to another. Thereby one has to distinguish between the cases of parallel [Fig. 2(a)] and antiparallel [Fig. 2(b)] spin orientations. In the latter case, the moving oxygen hole flips the spins on the copper sites and thus destroys their antiferromagnetic order. The second-order terms can both be combined and expressed in form of a Kondo-lattice Hamiltonian (see, for example, Ref. 14). Obviously oxygen holes can propagate even in the case of vanishing direct O-O hopping, i.e., for $t_{pp} = 0$. The indirect O-O hopping proportional to t_{pd}^2/Δ modifies the band structure given by H'_0 . Thus, the second-order exchange processes have to be included in the unperturbed Hamiltonian, at least approximately. For that reason we construct an exchange Hamiltonian H_{ex} , which is added to the unperturbed part $H_0 = H'_0 + H_{ex}$ and subtracted again from the perturbation $H_1 = H'_1 - H_{ex}$. With this the final partition of the Hamiltonian H into H_0 and H_1 is fixed.

In order to obtain an effective exchange operator H_{ex} which can easily be diagonalized we apply a mean-field approximation to the aforementioned Kondo-lattice Hamiltonian. Thereby the spin-flip terms are eliminated. This kind of approach is well justified if the direct hopping between oxygen sites exceeds the indirect one via copper sites, that is if $t_{pp} \gg t_{pd}^2/\Delta$. When expressed in the basis of the creation operators $p_{ik\sigma}^\dagger$ and $d_{ak\sigma}^\dagger$ the

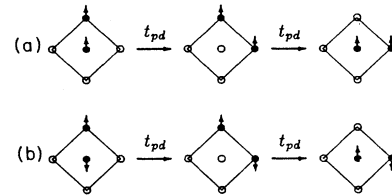


FIG. 2. Second-order exchange processes of an oxygen hole with up spin and a copper hole with parallel (a) or antiparallel (b) spin direction. The exchange leads to an effective propagation of oxygen holes.

Hamiltonian H_{ex} takes the form

$$H_{\text{ex}} = -\frac{4t_{pd}^2}{\Delta'} \sum_{\alpha k \sigma} \hat{d}_{\alpha k \sigma}^\dagger \hat{d}_{\alpha k \sigma} + \frac{t_{pd}^2}{\Delta'} \sum_{ij\mathbf{k}} \varphi_i \varphi_j (e^{i\mathbf{k}(\mathbf{r}_i - \mathbf{r}_j)} p_{i\mathbf{k}\uparrow}^\dagger p_{j\mathbf{k}\uparrow} + e^{-i\mathbf{k}(\mathbf{r}_i - \mathbf{r}_j)} p_{i\mathbf{k}\downarrow}^\dagger p_{j\mathbf{k}\downarrow}), \quad (23)$$

$$\Delta' = e_p - \epsilon_d = e_p - \frac{e_p + e_d}{2} + \sqrt{\frac{(e_p - e_d)^2}{4} + 4t_{pd}^2}.$$

The energy differences between oxygen bands and the copper level entering the denominators have been replaced by the average value Δ' . The terms in the second sum describe the effective hopping of oxygen holes without spin-flip processes as in Fig. 2(a). In second order there is also a back and forth hopping of holes between copper and oxygen states. These charge fluctuations of the ground state lower the copper energy from e_d to ϵ_d and are represented by the first sum. If we expand the Ω operator up to second order in t_{pd}/Δ the contribution from the effective Hamiltonian H_{ex} cancels the terms caused by exchange processes with parallel spin:

$$|\Omega\rangle_c = |1\rangle_c + \left| \frac{1}{-\mathcal{L}_o} H_1' \right\rangle_c + \frac{1}{-\mathcal{L}_o} \left[\left| H_1' \frac{1}{-\mathcal{L}_o} H_1' \right\rangle_c - |H_{\text{ex}}\rangle_c \right]. \quad (24)$$

Here, $|1\rangle_c$ denotes the ground state of H_0 . As it turns out, the corresponding exchange processes with spin flip, which are also present in the ground state, do not enter most of the frequency and susceptibility matrix elements and are neglected. Consequently, $|\Omega\rangle_c$ is given by the first two terms on the right-hand side of Eq. (24). The omission of the spin-flip processes in $|\Omega\rangle_c$ is justified, since we are not interested in ground-state properties of the Emery model but in the dynamics of added particles. In the dynamical part of the calculation, which depends crucially on the proper choice of projection operators, it is essential to maintain the exchange processes with spin flip. Thus they are only omitted in the static part of our approach, i.e., in the ground-state approximation but not in the dynamical part.

According to the definition of H_{ex} the diagonalization of the Hamilton operator $H_0 = H_0' + H_{\text{ex}}$ includes the second-order exchange processes with parallel spin orientation. We introduce new creation operators $c_{n\mathbf{k}\sigma}^\dagger$ for holes in oxygen bands $n=1, \dots, 4$ with energy $\epsilon_{n\mathbf{k}}$. Their coefficients in terms of the $p_{i\mathbf{k}\sigma}^\dagger$ are denoted by $\beta_{ni}(\mathbf{k})$. As abbreviations we use the phase factors $\phi_{n\mathbf{k}}$ and $\bar{\phi}_{n\mathbf{k}}$:

$$c_{n\mathbf{k}\uparrow}^\dagger = \sum_i \beta_{ni}(\mathbf{k}) p_{i\mathbf{k}\uparrow}^\dagger, \quad c_{n\mathbf{k}\downarrow}^\dagger = \sum_i \beta_{ni}^*(\mathbf{k}) p_{i\mathbf{k}\downarrow}^\dagger, \quad (25)$$

$$\phi_{n\mathbf{k}} = \frac{1}{2} \sum_{i=1}^4 \varphi_i e^{-i\mathbf{k}\cdot\mathbf{r}_i} \beta_{ni}(\mathbf{k}), \quad (26)$$

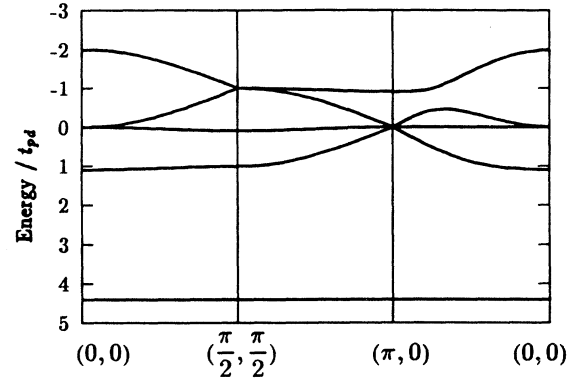


FIG. 3. Band structure of the unperturbed Hamiltonian H_0 for the parameter values $t_{pp} = 0.5$, $\Delta = 3.5$, and $t_{pd} = 1$ taken as the unit of energy. All \mathbf{k} points on the horizontal axis lie in the antiferromagnetic Brillouin zone.

$$\bar{\phi}_{n\mathbf{k}} = \frac{1}{2} \sum_{i=1}^4 \varphi_i e^{-i\mathbf{k}\cdot\mathbf{r}_i} \beta_{ni}^*(\mathbf{k}). \quad (27)$$

The Hamiltonian H_0 becomes diagonal with respect to the operators $c_{n\mathbf{k}\sigma}^\dagger$. Since it is convenient to use that representation of oxygen operators in the further calculations we also express the remaining operators H_1' and H_{ex} in that basis:

$$H_0 = \epsilon_d \sum_{\alpha k \sigma} \hat{d}_{\alpha k \sigma}^\dagger \hat{d}_{\alpha k \sigma} + \sum_{n\mathbf{k}\sigma} \epsilon_{n\mathbf{k}} c_{n\mathbf{k}\sigma}^\dagger c_{n\mathbf{k}\sigma}, \quad (28)$$

$$H_1' = \sum_{\alpha n\mathbf{k}\sigma} \left(T_{\alpha n\mathbf{k}\sigma}^{pd} \hat{d}_{\alpha k \sigma}^\dagger c_{n\mathbf{k}\sigma} + (T_{\alpha n\mathbf{k}\sigma}^{pd})^* c_{n\mathbf{k}\sigma}^\dagger \hat{d}_{\alpha k \sigma} \right), \quad (29)$$

$$H_{\text{ex}} = \sum_{m n\mathbf{k}\sigma} T_{m n\mathbf{k}\sigma}^{\text{ex}} c_{m\mathbf{k}\sigma}^\dagger c_{n\mathbf{k}\sigma} - \frac{4t_{pd}^2}{\Delta'} \sum_{\alpha k \sigma} \hat{d}_{\alpha k \sigma}^\dagger \hat{d}_{\alpha k \sigma}. \quad (30)$$

The corresponding matrix elements $T_{\alpha m\mathbf{k}\sigma}^{pd}$ and $T_{m n\mathbf{k}\sigma}^{\text{ex}}$ are given by

$$T_{\alpha m\mathbf{k}\sigma}^{pd} = -2t_{pd}\varphi_\alpha \{ \phi_{m\mathbf{k}} \delta_{\alpha A} \delta_{\sigma\uparrow} + \bar{\phi}_{m\mathbf{k}} \delta_{\alpha A} \delta_{\sigma\downarrow} + \bar{\phi}_{m\mathbf{k}}^* \delta_{\alpha B} \delta_{\sigma\uparrow} + \phi_{m\mathbf{k}}^* \delta_{\alpha B} \delta_{\sigma\downarrow} \}, \quad (31)$$

$$T_{m n\mathbf{k}\sigma}^{\text{ex}} = \frac{4t_{pd}^2}{\Delta'} (\phi_{m\mathbf{k}} \phi_{n\mathbf{k}}^* \delta_{\sigma\uparrow} + \phi_{m\mathbf{k}}^* \phi_{n\mathbf{k}} \delta_{\sigma\downarrow}). \quad (32)$$

In Fig. 3 the band structure of H_0 is plotted for the parameter values $t_{pp} = 0.5$, $e_p = 0$, and $e_d = -3.5$. For better comparison with the following quasiparticle dispersion curves the scale on the vertical axis refers to electronic energies (opposite sign). The copper level is shifted from 3.5 to higher energies due to the inclusion of ground-state fluctuations in H_0 . Compared to the bare oxygen band structure of H_0' , the highest oxygen band is much flatter. At the same time the band maximum increases from $4t_{pp}$ to 1.2. Consequently, the distance between the copper level and the band maximum is significantly enlarged through the action of H_{ex} and the expansion parameter $t_{pd}/\Delta' \approx \frac{1}{4}$ has become smaller. As regards to the ground state the application of H_1' in the second term on the right-hand side of Eq. (24) transfers

a part of the copper holes into unoccupied oxygen states. Thus, the hole occupation number of copper sites n_d at half-filling deviates from one. Using $\Delta = 3.0$ we find $n_d = 0.85$ for $t_{pp} = 0$ and $n_d = 0.73$ for $t_{pp} = 0.5$.

V. PHOTOEMISSION SPECTRA

In the sudden approximation the photoemission and inverse photoemission spectra are given by the one-hole spectral densities. With regard to photoemission we will consider the following correlation functions G_{mn}^p , $m, n \in \{1, \dots, 4\}$, and G_α^d , $\alpha \in \{A, B\}$, for oxygen and copper holes, respectively:

$$G_{mn}^p(\mathbf{k}, \omega) = \langle \Omega | c_{m\mathbf{k}\uparrow} \left(\frac{1}{\omega - \mathcal{L}} c_{n\mathbf{k}\uparrow}^\dagger \right) | \Omega \rangle_c, \quad (33)$$

$$G_\alpha^d(\mathbf{k}, \omega) = \langle \Omega | \hat{d}_{\alpha\mathbf{k}\uparrow} \left(\frac{1}{\omega - \mathcal{L}} \hat{d}_{\alpha\mathbf{k}\uparrow}^\dagger \right) | \Omega \rangle_c. \quad (34)$$

According to Eqs. (15) and (17) these dynamical correlation functions are evaluated by inserting a projector \mathcal{P} . We will use the same projector for both, G_{mn}^p and G_α^d . Therefore, the corresponding matrix equations differ only in the selection of the coupling terms \mathbf{c}^p and \mathbf{c}^d :

$$\underline{G}^p(\mathbf{k}, \omega) = [\underline{\mathbf{c}}^p(\mathbf{k})]^\dagger [\omega \cdot \underline{\chi}(\mathbf{k}) - \underline{\mathbf{F}}(\mathbf{k})]^{-1} \underline{\mathbf{c}}^p(\mathbf{k}), \quad (35)$$

$$c_{mn}^p(\mathbf{k}) = \langle \Omega | A_m^\dagger(\mathbf{k}) c_{n\mathbf{k}\uparrow}^\dagger | \Omega \rangle_c, \quad (36)$$

$$\underline{G}^d(\mathbf{k}, \omega) = [\underline{\mathbf{c}}^d(\mathbf{k})]^\dagger [\omega \cdot \underline{\chi}(\mathbf{k}) - \underline{\mathbf{F}}(\mathbf{k})]^{-1} \underline{\mathbf{c}}^d(\mathbf{k}), \quad (37)$$

$$c_{m\alpha}^d(\mathbf{k}) = \langle \Omega | A_m^\dagger(\mathbf{k}) \hat{d}_{\alpha\mathbf{k}\uparrow}^\dagger | \Omega \rangle_c. \quad (38)$$

The frequency matrix $\underline{\mathbf{F}}(\mathbf{k})$ and the susceptibility matrix $\underline{\chi}(\mathbf{k})$ are given by Eqs. (19) and (16), respectively.

We now turn our attention to the choice of the projectors A_m . Our search for appropriate operators is guided by two principles: First the chosen set should couple in the frequency matrix $\underline{\mathbf{F}}$ to the hole creation operators $c_{n\mathbf{k}\uparrow}^\dagger$ or $\hat{d}_{\alpha\mathbf{k}\uparrow}^\dagger$ since the latter generate the initial configurations in Eqs. (33) and (34). Therefore, the projection operators A_m are determined by calculating successively the commutators $\mathcal{L}'_1 c_{n\mathbf{k}\uparrow}^\dagger$, $(\mathcal{L}'_1)^2 c_{n\mathbf{k}\uparrow}^\dagger$, $(\mathcal{L}'_1)^3 c_{n\mathbf{k}\uparrow}^\dagger$, etc. Second, one has to make sure that the corresponding susceptibility matrix $\underline{\chi}$ is positive definite. Due to the use of cumulants this is not obvious. If $A = X_1 X_2$ replaces a product of operators X_1, X_2 subjected to cumulant formation, an expression of the form $\langle A^\dagger A \rangle_c$ is not necessarily positive. But this feature does not pose strong restrictions on the choice of operators A_m .

The projection operator \mathcal{P} for the photoemission spectra contains four different types of operators A_m :

$$A_n(\mathbf{k}) = c_{n\mathbf{k}\uparrow}^\dagger, \quad n = 1, \dots, 4, \quad \text{if } \epsilon_{n\mathbf{k}} > \epsilon_F, \quad (39)$$

$$A_5(\mathbf{k}, \mathbf{q}) = p_{B\mathbf{q}\downarrow}^\dagger S_{B(\mathbf{k}-\mathbf{q})}^+, \quad \text{if } \epsilon_{1\mathbf{q}} > \epsilon_F, \quad (40)$$

$$A_6(\mathbf{k}) = \frac{1}{N} \sum_{\mathbf{q}_1 \mathbf{q}_2} p_{B\mathbf{q}_1\downarrow}^\dagger p_{B\mathbf{q}_2\uparrow}^\dagger \hat{d}_{B(\mathbf{q}_1+\mathbf{q}_2-\mathbf{k})\downarrow}, \quad (41)$$

$$A_7(\mathbf{k}) = \frac{2}{N} \sum_{m\mathbf{q}_1 \mathbf{q}_2} \phi_{m\mathbf{q}_1} \bar{\phi}_{m\mathbf{q}_1} p_{A\mathbf{q}_2\uparrow}^\dagger S_{A(\mathbf{q}_2-\mathbf{q}_1)}^- S_{B(\mathbf{k}-\mathbf{q}_1)}^+. \quad (42)$$

In this set of equations, ϵ_F denotes the Fermi energy of the unperturbed system, N is the number of lattice cells, and the spin-flip operators $S_{\alpha\mathbf{k}}^+$ are defined through the relations

$$S_{\alpha\mathbf{k}}^+ = \frac{1}{\sqrt{N}} \sum_I e^{-i\mathbf{k} \cdot \mathbf{R}_{I\alpha}} S_{\alpha I}^+, \quad (43)$$

where $S_{\alpha I}^+ = d_{\alpha I\uparrow}^\dagger d_{\alpha I\downarrow}$. The operators $A_1(\mathbf{k}), \dots, A_4(\mathbf{k})$ generate an oxygen hole with up spin in one of the four bands m . Thereby the corresponding state has to be unoccupied in the unperturbed ground state since otherwise the susceptibility matrix element $\chi_{mm}(\mathbf{k})$ vanishes.

The next type of operator $A_5(\mathbf{k}, \mathbf{q})$ consists of an oxygen hole with flipped spin in a symmetric state and a spin-wave excitation in the B sublattice. Roughly speaking, the set of operators $A_5(\mathbf{k}, \mathbf{q})$ represents the third configuration in Fig. 2(b). This is seen by introducing the integrated operator $A_5(\mathbf{k})$:

$$A_5(\mathbf{k}) = \frac{1}{\sqrt{N}} \sum_{\mathbf{q}} A_5(\mathbf{k}, \mathbf{q}) = \frac{1}{\sqrt{N}} \sum_I e^{-i\mathbf{k} \cdot \mathbf{R}_{IB}} p_{BI\downarrow}^\dagger S_{BI}^+. \quad (44)$$

If the operator $p_{BI\downarrow}^\dagger S_{BI}^+$ is applied to the Néel state the final configuration of Fig. 2(b) arises. In the frequency matrix, the operator $A_5(\mathbf{k})$ couples to $A_1(\mathbf{k}), \dots, A_4(\mathbf{k})$ through the exchange processes with spin flip. We have decomposed the spin-flip operator $A_5(\mathbf{k})$ into single \mathbf{q} components since, as before, the susceptibility matrix elements referring to occupied oxygen band states vanish.

As mentioned before, all projectors A_m are constructed by considering the commutators $(\mathcal{L}'_1)^n c_{m\mathbf{k}\uparrow}^\dagger$. The expression for $n = 1$, $\mathcal{L}'_1 c_{m\mathbf{k}\uparrow}^\dagger$, leads to the copper creation operators $\hat{d}_{\alpha\mathbf{k}\uparrow}^\dagger$. The spin-flip operators $A_5(\mathbf{k}, \mathbf{q})$ then appear as a component of $\mathcal{L}'_1 \hat{d}_{\alpha\mathbf{k}\uparrow}^\dagger$. Some relevant commutators are shown in Appendix A. $A_6(\mathbf{k})$ is a part of the commutator $\mathcal{L}'_1 A_5(\mathbf{k})$. It can be called a dynamical charge excitation operator.

Finally, $A_7(\mathbf{k})$ is found by considering $(\mathcal{L}'_1)^2 A_5(\mathbf{k})$. As one realizes by inspection of Fig. 2(b), a propagating oxygen hole successively flips more and more copper spins. The configuration produced by $A_5(\mathbf{k})$ is only the beginning step. $A_7(\mathbf{k})$ generates a succeeding state with a string of two overturned spins. The projectors $A_1(\mathbf{k}), \dots, A_7(\mathbf{k})$ coincide at half-filling with the operator set used in Ref. 6 if the operator type $A_5(\mathbf{k}, \mathbf{q})$ is replaced by its integrated version $A_5(\mathbf{k})$.

One might ask why we have not also included the creation operators of copper holes $\hat{d}_{\alpha\mathbf{k}\uparrow}^\dagger$ in the list of projectors in Eqs. (39)–(42). However, such a choice proves to be unfavorable due to the fact that in the susceptibility matrix $\underline{\chi}$ the corresponding diagonal elements are small, whereas the overlap with the oxygen operators $c_{m\mathbf{k}\uparrow}^\dagger$ is not. Due to the large overlap between copper and oxygen it is easier to determine the photoemission spectrum of copper holes solely through their coupling in \mathbf{c}^d to the operators $A_1(\mathbf{k}), \dots, A_4(\mathbf{k})$.

With respect to the set of projection operators of

Eq. (39) we calculated the frequency and susceptibility matrix elements using the ground-state approximation of Sec. IV. The results are found in Appendix B. Numerically, the spectra are evaluated by diagonalizing $\underline{F}(\mathbf{k})$ and $\underline{\chi}(\mathbf{k})$ at all \mathbf{k} points of a rectangular net in the antiferromagnetic Brillouin zone. For a fixed \mathbf{k} point, $A_5(\mathbf{k}, \mathbf{q})$ operators are taken into account at those \mathbf{q} points of the net which are unoccupied (i.e., for $\epsilon_{1\mathbf{q}} > \epsilon_F$).

In Fig. 4, the photoemission spectra of oxygen and copper holes at half-filling are presented for the parameter values $t_{pp} = 0$ and $\Delta = 3$. In the following $t_{pd} = 1$ is taken as the unit of energy. The spectra are integrated in reciprocal space and refer to the local creation of an oxygen hole $p_{1I\uparrow}^\dagger$ or a copper hole $1/\sqrt{2}(d_{AI\uparrow}^\dagger + d_{BI\uparrow}^\dagger)$. The dominant maximum in the oxygen spectrum at $\omega = 0$ consists of antisymmetric linear combinations of oxygen orbitals which do not couple to copper holes. Therefore they form a dispersionless, nonbonding band for $t_{pp} = 0$. As a consequence of strong correlations in the Emery model the remaining spectral density is dominated by two-particle states, which are absent in any type of mean-field description. In real space, they are formed by the symmetric linear combination $p_{\alpha I\sigma}^\dagger$ and the d orbital in the center. The lowest unoccupied states at $\omega = 1.0$ in Fig. 4 are singlets. The corresponding triplets appear in the energy range between $\omega = -0.5$ and $\omega = -1.0$. They hybridize with two bands and lead therefore to a double peak structure. The eigenoperators $S(\mathbf{k})$ and $T(\mathbf{k})$, belonging to the singlet and triplet maxima for a given \mathbf{k} point, are roughly of the form

$$S(\mathbf{k}) = \frac{1}{\sqrt{2}} \left(p_{B\mathbf{k}\uparrow}^\dagger - \frac{1}{\sqrt{N_u}} \sum_{\mathbf{q}}^{\text{unocc}} p_{B\mathbf{q}\downarrow}^\dagger S_{B(\mathbf{k}-\mathbf{q})}^+ \right), \quad (45)$$

$$T(\mathbf{k}) = \frac{1}{\sqrt{2}} \left(p_{B\mathbf{k}\uparrow}^\dagger + \frac{1}{\sqrt{N_u}} \sum_{\mathbf{q}}^{\text{unocc}} p_{B\mathbf{q}\downarrow}^\dagger S_{B(\mathbf{k}-\mathbf{q})}^+ \right). \quad (46)$$

Thereby, N_u is the number of unoccupied \mathbf{k} points (with $\epsilon_{1\mathbf{k}} > \epsilon_F$). As can be seen, $S(\mathbf{k})$ and $T(\mathbf{k})$ are linear combinations of the projectors $A_1(\mathbf{k}), \dots, A_4(\mathbf{k})$ and $A_5(\mathbf{k}, \mathbf{q})$. One should point out, however, that there is also an admixture of the remaining two operator types

$A_6(\mathbf{k})$ and $A_7(\mathbf{k})$, which is shifting the singlet position to higher energies. At $\omega = -2.6$ one finds a weak maximum due to the string operator $A_7(\mathbf{k})$. The small peak referring to $A_6(\mathbf{k})$ appears first at $\omega = -6.2$, outside the energy range of Fig. 4. The photoemission spectrum for copper holes contains only the singlet and triplet maxima since there is no coupling to the antisymmetric oxygen states at $\omega = 0$. We find for the singlet peak 80% oxygen and 20% copper weight.

As has been recognized by Zhang and Rice,¹⁵ the lowest unoccupied hole states (with respect to half-filling) in the Emery model are singlets. Within one B plaquette of oxygen orbitals surrounding the central copper site the singlet is of the form

$$S = \frac{1}{\sqrt{2}} (p_{BI\uparrow}^\dagger d_{BI\downarrow}^\dagger - p_{BI\downarrow}^\dagger d_{BI\uparrow}^\dagger). \quad (47)$$

If $S(\mathbf{k})$ of Eq. (45) acts on the Néel state of the copper spins, a singlet with wave vector \mathbf{k} is generated. On a B plaquette it is described by Eq. (47). The considerations of Zhang and Rice have also been confirmed by exact diagonalization studies of small copper-oxygen clusters with periodic boundary conditions.^{4,5,7,16,17} Our photoemission spectra are in good agreement with these calculations. This statement refers not only to the appearance of singlet and triplet states in the spectra but also to the peak positions and intensities. One difference is the fact that the triplet states are distributed over two bands, which are either not present or cannot be resolved in the calculations for small clusters.

When the direct O-O hopping t_{pp} is turned on, the large maximum of nonbonding states in the oxygen spectrum transforms into a broad structure of band states. This can be seen in Fig. 5, where we have used the parameter values $t_{pp} = 0.6$ and $\Delta = 4$. Although the largest peak in the oxygen spectrum remains close to $\omega = 0$ its physical origin is different. Now this maximum is formed by triplet states, which have been shifted together with the singlet states to higher energies. The described trend is reflected in the form of the copper spectrum. The bandwidth of the singlet states is only weakly affected by the O-O hopping and remains to be small. However,

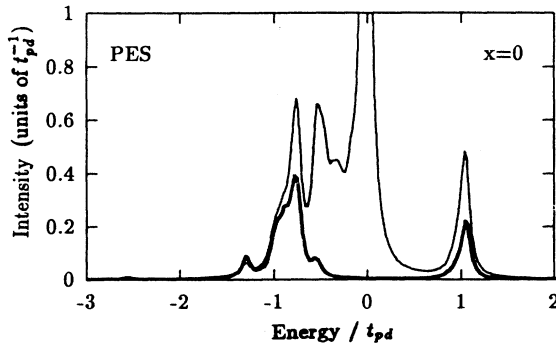


FIG. 4. Photoemission spectra (PES) of oxygen holes (thin line) and copper holes (thick line) at half-filling ($x=0$). The parameter values are $t_{pp} = 0$ and $\Delta = 3$.

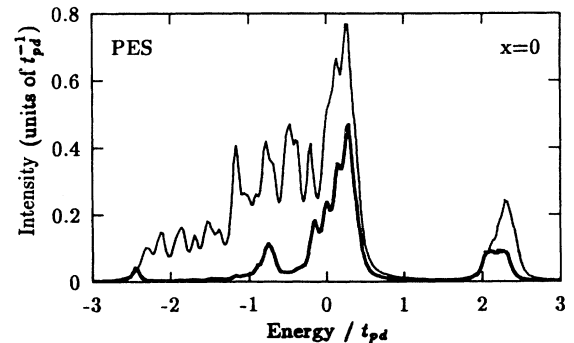


FIG. 5. Photoemission spectra of oxygen holes (thin line) and copper holes (thick line) at half-filling ($x=0$). The parameter values are $t_{pp} = 0.6$ and $\Delta = 4$.

the overall width of the spectrum clearly has increased.

After the discussion of the photoemission spectra we turn our attention to the inverse problem. Another subject of the next section is the change in the spectral densities for increasing hole concentration.

VI. INVERSE PHOTOEMISSION SPECTRA

To determine the inverse photoemission spectra of oxygen and copper holes in the Emery model we proceed similarly as in the last section. We start out by introducing the dynamical correlation functions $\overline{G}_{mn}^p(\mathbf{k}, \omega)$, $m, n \in \{1, \dots, 4\}$, and $\overline{G}_\alpha^d(\mathbf{k}, \omega)$, $\alpha \in \{A, B\}$. All quantities of the inverse spectra will be marked by overlined symbols:

$$\overline{G}_{mn}^p(\mathbf{k}, \omega) = \langle \Omega | c_{m\mathbf{k}\uparrow}^\dagger \left(\frac{1}{\omega - \mathcal{L}} c_{n\mathbf{k}\uparrow} \right) | \Omega \rangle_c, \quad (48)$$

$$\overline{G}_\alpha^d(\mathbf{k}, \omega) = \langle \Omega | \hat{d}_{\alpha\mathbf{k}\uparrow}^\dagger \left(\frac{1}{\omega - \mathcal{L}} \hat{d}_{\alpha\mathbf{k}\uparrow} \right) | \Omega \rangle_c. \quad (49)$$

These relations are again expressed in form of simple matrix equations by inserting the projection operator $\overline{\mathcal{P}}$ as done in Eq. (17):

$$\overline{\mathcal{P}} = \sum_{m,n} | \overline{A}_m \Omega \rangle_c \overline{\chi}_{mn}^{-1} \langle \Omega \overline{A}_n |. \quad (50)$$

The pole positions of the correlation functions $\overline{G}_{mn}^p(\mathbf{k}, \omega)$ and $\overline{G}_\alpha^d(\mathbf{k}, \omega)$ follow from the corresponding susceptibility and frequency matrices $\overline{\chi}$ and \overline{F} . The coupling terms $\overline{c}^p(\mathbf{k})$ or $\overline{c}^d(\mathbf{k})$ influence merely their weights in the spectral densities of oxygen or copper holes:

$$\overline{\mathcal{G}}^p(\mathbf{k}, \omega) = [\overline{c}^p(\mathbf{k})]^\dagger [\omega \cdot \overline{\chi}(\mathbf{k}) - \overline{F}(\mathbf{k})]^{-1} \overline{c}^p(\mathbf{k}), \quad (51)$$

$$\overline{c}_{mn}^p(\mathbf{k}) = \langle \Omega | \overline{A}_m^\dagger(\mathbf{k}) c_{n\mathbf{k}\uparrow} | \Omega \rangle_c, \quad (52)$$

$$\overline{\mathcal{G}}^d(\mathbf{k}, \omega) = [\overline{c}^d(\mathbf{k})]^\dagger [\omega \cdot \overline{\chi}(\mathbf{k}) - \overline{F}(\mathbf{k})]^{-1} \overline{c}^d(\mathbf{k}), \quad (53)$$

$$\overline{c}_{m\alpha}^d(\mathbf{k}) = \langle \Omega | \overline{A}_m^\dagger(\mathbf{k}) \hat{d}_{\alpha\mathbf{k}\uparrow} | \Omega \rangle_c. \quad (54)$$

The frequency matrix $\overline{F}(\mathbf{k})$ and the susceptibility matrix $\overline{\chi}(\mathbf{k})$ are defined through Eqs. (19) and (16), respectively, if we replace the operators A_m by the corresponding projectors of the inverse spectra \overline{A}_m .

Four different types of projectors enter the calculation of the inverse photoemission spectra:

$$\overline{A}_1(\mathbf{k}) = \hat{d}_{A\mathbf{k}\uparrow}, \quad (55)$$

$$\overline{A}_2(\mathbf{k}, \mathbf{q}) = \begin{cases} p_{A\mathbf{q}\downarrow} S_{A(\mathbf{k}-\mathbf{q})}^- & \epsilon_{1\mathbf{k}} > \epsilon_F, \\ \frac{1}{\sqrt{2}} \left(\frac{1}{\sqrt{N_o}} p_{A\mathbf{k}\uparrow} - p_{A\mathbf{q}\downarrow} S_{A(\mathbf{k}-\mathbf{q})}^- \right) & \epsilon_{1\mathbf{k}} \leq \epsilon_F, \\ \text{for all } \mathbf{q} \text{ with } \epsilon_{1\mathbf{q}} \leq \epsilon_F, & \end{cases} \quad (56)$$

$$\overline{A}_3(\mathbf{k}) = \frac{2}{\sqrt{N}} \sum_{m\mathbf{q}} \phi_{m\mathbf{q}} \overline{\phi}_{m\mathbf{q}} \hat{d}_{B\mathbf{q}\downarrow} S_{A(\mathbf{k}-\mathbf{q})}^-. \quad (57)$$

Thereby the operator $\overline{A}_2(\mathbf{k}, \mathbf{q})$ is split into two different expressions. In the first case, $\epsilon_{1\mathbf{k}} > \epsilon_F$, the four oxygen band states at point \mathbf{k} are unoccupied, whereas in the sec-

ond case, $\epsilon_{1\mathbf{k}} \leq \epsilon_F$, an additional hole occupies the lowest oxygen band state. For small doping concentrations considered here the higher oxygen bands $m = 2, 3, 4$, remain always empty. The variable N_o denotes the number of occupied \mathbf{k} points.

\overline{A}_1 represents the annihilation operator of copper holes on A sites. The corresponding operator for B sites, $\hat{d}_{B\mathbf{k}\uparrow}$, drops out of the calculation because its susceptibility matrix element vanishes. This is due to the fact that within the approximation made for the ground state there are no copper holes with spin direction opposite to the Néel order. For the same reason, there is no contribution from the correlation function $\overline{G}_B^d(\mathbf{k}, \omega)$ to the inverse spectral density. The operator $\hat{d}_{A\mathbf{k}\uparrow}$ is a good starting point for the construction of the remaining projection operators \overline{A}_m . Similar as in the case of the photoemission spectra they are determined by calculating the commutators $\mathcal{L}'_1 \hat{d}_{A\mathbf{k}\uparrow}$ and $(\mathcal{L}'_1)^2 \hat{d}_{A\mathbf{k}\uparrow}$. The results are shown in Appendix A.

In the commutator $\mathcal{L}'_1 \hat{d}_{A\mathbf{k}\uparrow}$ two relevant types of projection operators appear:

$$\overline{A}'_2(\mathbf{k}) = p_{A\mathbf{k}\uparrow}, \quad (58)$$

$$\overline{A}''_2(\mathbf{k}, \mathbf{q}) = p_{A\mathbf{q}\downarrow} S_{A(\mathbf{k}-\mathbf{q})}^-. \quad (59)$$

The first one, $\overline{A}'_2(\mathbf{k})$, describes the annihilation of an oxygen hole in a symmetric state with respect to the A plaquette. For the corresponding susceptibility matrix element to be sufficiently large, a high occupation number of the state to which $p_{A\mathbf{k}\uparrow}$ is applied is necessary. If $\epsilon_{1\mathbf{k}} \leq \epsilon_F$ this condition is fulfilled since the lowest oxygen band states are highly symmetric for $t_{pp} > t_{pd}^2/\Delta$. In the opposite case, i.e., $\epsilon_{1\mathbf{k}} > \epsilon_F$, the possibility to annihilate oxygen holes with momentum \mathbf{k} arises solely through the presence of charge fluctuations in the ground state. Therefore, the corresponding susceptibility matrix element is small and the operator $\overline{A}'_2(\mathbf{k})$ appears to be irrelevant. The second projector $\overline{A}''_2(\mathbf{k}, \mathbf{q})$ resembles the spin-flip operator $A_5(\mathbf{k}, \mathbf{q})$ considered previously [Eq. (40)]. Here, it represents a spin-wave excitation on sublattice A together with a symmetric superposition of oxygen holes on an A plaquette, $p_{A\mathbf{q}\downarrow}$. For the same reasons, $\overline{A}''_2(\mathbf{k}, \mathbf{q})$ is only a relevant operator in case of $\epsilon_{1\mathbf{q}} \leq \epsilon_F$.

If the operators $\overline{A}'_2(\mathbf{k})$ and $\overline{A}''_2(\mathbf{k}, \mathbf{q})$ at an occupied \mathbf{k} point ($\epsilon_{1\mathbf{k}} \leq \epsilon_F$) are applied separately as projectors the diagonalization of the corresponding frequency and susceptibility matrices creates the eigenoperators $\overline{S}(\mathbf{k})$ and $\overline{T}(\mathbf{k})$:

$$\overline{S}(\mathbf{k}) = \frac{1}{\sqrt{2}} \left(p_{A\mathbf{k}\uparrow} - \frac{1}{\sqrt{N_o}} \sum_{\mathbf{q}}^{\text{occ}} p_{A\mathbf{q}\downarrow} S_{A(\mathbf{k}-\mathbf{q})}^- \right), \quad (60)$$

$$\overline{T}(\mathbf{k}) = \frac{1}{\sqrt{2}} \left(p_{A\mathbf{k}\uparrow} + \frac{1}{\sqrt{N_o}} \sum_{\mathbf{q}}^{\text{occ}} p_{A\mathbf{q}\downarrow} S_{A(\mathbf{k}-\mathbf{q})}^- \right). \quad (61)$$

$\overline{S}(\mathbf{k})$ and $\overline{T}(\mathbf{k})$ are annihilation operators of holes in singlet or triplet states. Their pole positions coincide with the corresponding eigenvalues of the singlet and triplet

linear combinations $S(\mathbf{k})$ and $T(\mathbf{k})$ [Eqs. (45) and (46)]. The singlet maxima due to $\bar{S}(\mathbf{k})$ appear in the inverse spectral densities as soon as the system is doped with holes. They join directly the singlet peaks in the photoemission spectra. This behavior reflects the fact that the additional oxygen holes occupy the lowest energy states of the strongly correlated system, namely, the singlet states. Therefore, these singlet states can be annihilated causing peak structures adjacent to the photoemission spectrum. We do not consider the triplet operators any further. Otherwise we should work with an improved approximation for the ground state. For that reason we have chosen at occupied \mathbf{k} points (with $\epsilon_{1\mathbf{k}} \leq \epsilon_F$) a superposition of the operators $p_{A\mathbf{k}\uparrow}$ and $p_{A\mathbf{q}\downarrow} S_{A(\mathbf{k}-\mathbf{q})}^-$ allowing only for the singlet formation. At unoccupied \mathbf{k} points ($\epsilon_{1\mathbf{k}} > \epsilon_F$), we use the spin-flip operators $\bar{A}_2''(\mathbf{k}, \mathbf{q})$ only, since, as discussed before, the operators $\bar{A}_2(\mathbf{k})$ are not relevant in that case.

The remaining projection operator $\bar{A}_3(\mathbf{k})$ is obtained starting out from an integrated version of the spin-flip operator $\bar{A}_2''(\mathbf{k}, \mathbf{q})$:

$$\bar{A}_2''(\mathbf{k}) = \frac{1}{\sqrt{N}} \sum_{\mathbf{q}} p_{A\mathbf{q}\downarrow} S_{A(\mathbf{k}-\mathbf{q})}^- \quad (62)$$

$\bar{A}_3(\mathbf{k})$ arises as a part of the commutator $\mathcal{L}'_1 \bar{A}_2''(\mathbf{k})$, which is shown in Appendix A. A copper hole on the sublattice B is accompanied by a spin-wave excitation. Therefore, $\bar{A}_3(\mathbf{k})$ may be called spin-flip operator for copper holes.

The bare annihilation operators of oxygen holes $c_{m\mathbf{k}\uparrow}$ enter the set of projectors \bar{A}_m solely in form of the symmetric linear combination $p_{A\mathbf{k}\uparrow}$ for $\epsilon_{1\mathbf{k}} \leq \epsilon_F$ as a component of $\bar{A}_2(\mathbf{k}, \mathbf{q})$ [Eq. (56)]. The corresponding anti-symmetric linear combinations are useless as projection operators because they do not couple to the copper system. Thus, they are not occupied through the occurrence of charge fluctuations in the ground state and their susceptibility matrix elements disappear. For that reason, we are left with the symmetric linear combination $p_{A\mathbf{k}\uparrow}$. In case of $\epsilon_{1\mathbf{k}} > \epsilon_F$ the possibility to annihilate a symmetric oxygen hole is taken into account in the matrix \bar{c}^p as a coupling between the oxygen operators $c_{m\mathbf{k}\uparrow}$ and $\bar{A}_1(\mathbf{k})$. Therefore including $p_{A\mathbf{k}\uparrow}$ exclusively in $\bar{A}_2(\mathbf{k}, \mathbf{q})$ for $\epsilon_{1\mathbf{k}} \leq \epsilon_F$ turns out to be sufficient.

Figure 6 shows the photoemission spectra (left, thin lines) together with the inverse photoemission spectra (right, thick lines) of oxygen holes at half-filling and a doping rate of $x = 0.2$. We have chosen the parameters $t_{pp} = 0.6$ and $\Delta = 4$. The corresponding spectra for copper holes are presented in Fig. 7. Just as before, the spectral densities are integrated in reciprocal space. The intensities in the inverse spectra refer to the local annihilation operators $p_{1I\uparrow}$ and $1/\sqrt{2}(\hat{d}_{AI\uparrow} + \hat{d}_{BI\uparrow})$ for oxygen and copper holes, respectively.

We begin our discussion with the inverse spectra at half-filling. The most important result is the existence of an energy gap of width $\Delta\epsilon = 2$ between the photoemission and inverse photoemission spectra. It is limited in the inverse spectra at $\omega = 4.5$ by the upper Hubbard band. In the corresponding eigenoperators, the $\bar{A}_1(\mathbf{k})$ -

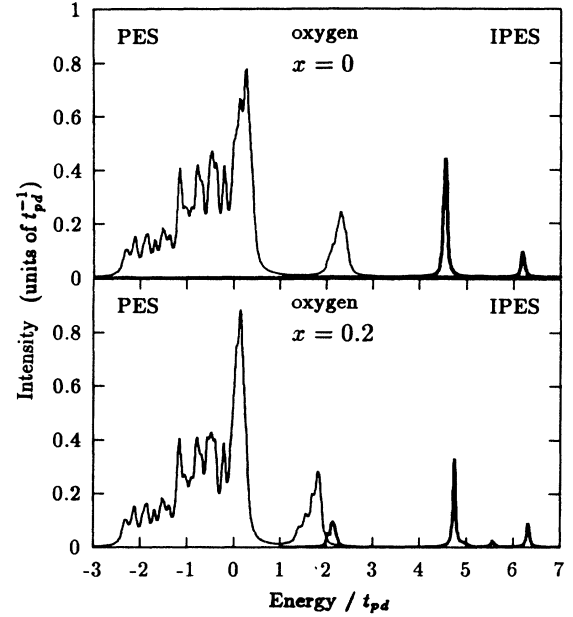


FIG. 6. Oxygen holes: Photoemission spectra (PES, thin lines) and inverse photoemission spectra (IPES, thick lines) for half-filling ($x=0$, above) and hole doping ($x=0.2$, below). Parameter values: $t_{pp} = 0.6$, $\Delta = 4$.

components are dominant. The appearance of a gap at half-filling is a remarkable consequence of the strong correlations in the Emery model, which turns out to be a charge transfer insulator. The eigenoperators of the second pole at $\omega = 6.2$ have a strong admixture of $\bar{A}_3(\mathbf{k})$.

If the system is doped with additional holes the energy

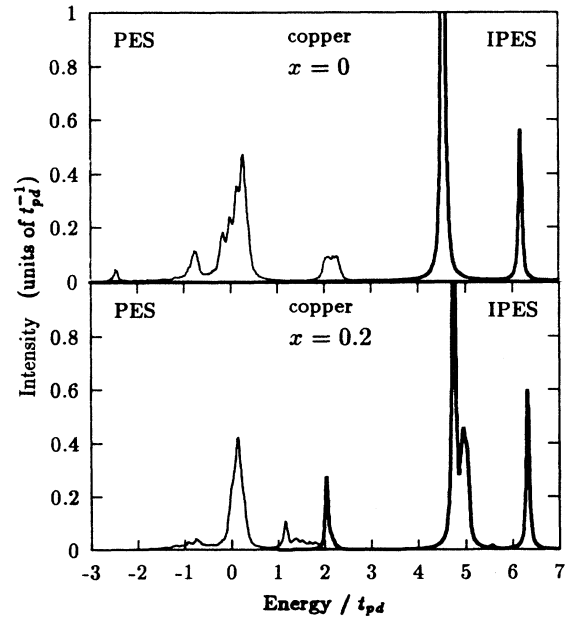


FIG. 7. Copper holes: Photoemission spectra (PES, thin lines) and inverse photoemission spectra (IPES, thick lines) for half-filling ($x=0$, above) and hole doping ($x=0.2$, below). Parameter values: $t_{pp} = 0.6$, $\Delta = 4$.

gap vanishes. This can be clearly seen in Figs. 6 and 7. In the inverse oxygen spectrum as well as in the inverse copper spectrum, new structures appear around an energy $\omega = 2$, joining directly the highest states of the photoemission spectrum. These structures result from new linear combinations of projectors which are of singlet character since the operators $\bar{A}_2(\mathbf{k}, \mathbf{q})$ have a large weight. Due to the fact that the holes in the states close to the Fermi energy are delocalized, the doped system shows metallic properties. In conclusion, the doping of the Emery model with holes leads to an insulator-to-metal transition. Comparing the spectra at half-filling and for finite hole doping reveals two additional many-particle effects: Firstly, under doping the position of the singlet poles as a whole moves to lower energies whereas the upper Hubbard band shows the opposite trend. Secondly, spectral weight is shifted from the outer regions of the hole spectral densities to states near the Fermi energy. We will discuss these observations in greater detail in the next section.

The insulator-to-metal transition in the Emery model as a consequence of hole doping has previously been found in exact diagonalization studies of small $(\text{CuO}_2)_4$ clusters.^{4,5,7,16,17} The basic form of the inverse spectral density shown in Figs. 6 and 7, namely, the singlet structure, the upper Hubbard band, and the smaller peak at high energies, coincides very well with the results of Tohyama and Maekawa¹⁶ for $t_{pp} = 0.4$. Furthermore, the shift of the singlet maxima and the upper Hubbard band, which are accompanied by a change of spectral weight, has also been found in the work of Eskes and co-workers.^{7,18}

VII. DISCUSSION

The influence of hole doping on the photoemission spectrum of oxygen holes can be seen in detail by considering Fig. 8. For comparison, the spectral densities at half-filling ($x = 0$, thick line) and for a doped system ($x = 0.2$, thin line) are shown. The parameter values $t_{pp} = 0.6$ and $\Delta = 4$ were used. Obviously, the dis-

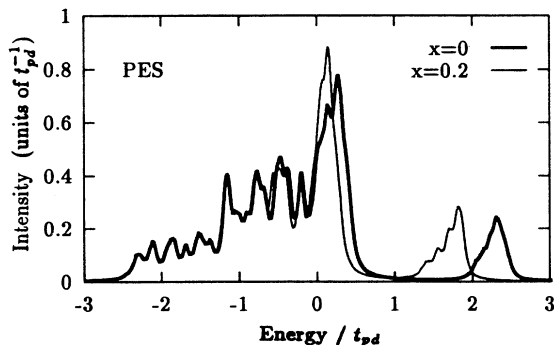


FIG. 8. Comparison of photoemission spectra for oxygen holes at half-filling ($x=0$, thick line) and hole doping ($x=0.2$, thin line). Parameter values: $t_{pp} = 0.6$, $\Delta = 4$. The singlet weight increases with doping.

tance between the singlet and the triplet peak is decreasing with doping. Thereby the triplet position remains nearly unchanged. At energies $\omega < 0$ the spectra are almost unaffected by the additional holes. According to a sum rule, the total weight of the oxygen spectra has to become smaller under doping. However, the spectral weight of the singlet states is not reduced as one would expect in a one-particle picture. On the contrary, the total spectral weight of the singlet states increases with hole doping although some of them are now occupied by additional holes and therefore disappear from the photoemission spectra. At $x = 0.2$ the total singlet intensity is about 20% larger than at half-filling. This kind of behavior is a surprising consequence of strong correlations between holes in the copper system.

The shift of the singlet maximum to lower energies and the increase of its spectral weight under doping are both of the same origin. As was mentioned before, the singlets are formed by a symmetric linear combination of operators $A_1(\mathbf{k}), \dots, A_4(\mathbf{k})$ with the spin-flip operators $A_5(\mathbf{k}, \mathbf{q})$ [Eq. (45)] at unoccupied \mathbf{q} points ($\epsilon_{1\mathbf{q}} > \epsilon_F$). With increasing doping the number of unoccupied \mathbf{q} points becomes smaller and the energy gain due to singlet formation decreases. Therefore, the singlets move in the direction of the oxygen orbital energy $e_p = 0$. The admixture of spin-flip operators $A_5(\mathbf{k}, \mathbf{q})$ to states close to the Fermi energy is diminished whereas the contribution of $A_1(\mathbf{k}), \dots, A_4(\mathbf{k})$ increases. This increase leads to a rise of the singlet weight in the oxygen spectrum. The gain in spectral weight overcompensates the loss caused through the occupation of the lowest singlet states by additional holes. As is seen in Fig. 8, also the maximum of the triplet states around $\omega = 0.2$ becomes more pronounced under doping.

In the inverse photoemission spectra, the strong correlations lead to similar effects. In Fig. 9 the inverse

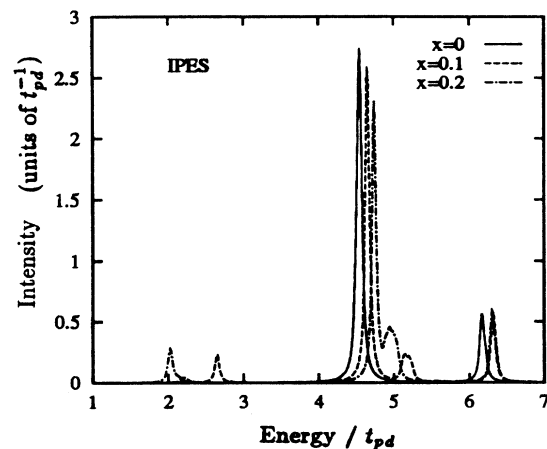


FIG. 9. Inverse photoemission spectra of copper holes for the hole concentrations $x=0$ (full), $x=0.1$, and $x=0.2$ (dashed). The parameter values are $t_{pp} = 0.6$ and $\Delta = 4$. The intensity of the upper Hubbard band decreases with growing hole concentration and spectral weight is shifted to the new states at the Fermi energy (on the left side). Simultaneously the distance between the singlet peaks and the upper Hubbard band increases.

spectrum of copper holes is shown for half-filling ($x = 0$, solid line) and for two doping concentrations ($x = 0.1$, $x = 0.2$, dashed lines). The same parameter values are used as in Fig. 8. At half-filling, the system has an energy gap and there are no states at the Fermi energy. When the system is doped, new states with singlet character arise in the energy range from $\omega = 2$ to $\omega = 3$ and the system undergoes an insulator-to-metal transition. As can be seen in Fig. 9, the states near the Fermi energy shift to lower energies with increasing hole concentrations. The same trend is found for the highest states in the photoemission spectra of Fig. 8. Simultaneously, the upper Hubbard band moves to slightly larger energies. Thereby its intensity decreases steadily. Since the total spectral weight of the inverse copper spectrum is given by the hole occupation number of copper sites n_d , it grows in case of hole doping. Clearly, the intensity of the singlet states close to the Fermi energy is becoming larger. But their weight is increasing more rapidly than the total spectral weight. For example, at a doping rate of $x = 0.1$ the singlet intensity exceeds the increase in n_d by 82%. To summarize one may say that hole doping leads to a shift of spectral weight from the upper Hubbard band to states close to the Fermi energy.

In Fig. 10, we show the dispersion of dominating quasi-particle poles in the photoemission (black dots) and inverse photoemission spectrum (circles) at half-filling ($t_{pp} = 0.6$, $\Delta = 4$). The \mathbf{k} points on the horizontal axis all lay within the antiferromagnetic Brillouin zone. The upper Hubbard band at $\omega = 4.5$ and the smaller peak at $\omega = 6.2$ in the inverse spectrum are nearly dispersionless. The energy gap between $2.5 \leq \omega \leq 4.5$ is limited in the photoemission spectrum by the flat singlet band. The corresponding triplet states between $0 \leq \omega \leq 0.5$ also show only a weak dispersion. By comparing with Fig. 3 it is noticed that the two bands with lowest energy have a similar form as found for the band structure of the Hamiltonian H_0 . One may conclude that the perturbation H_1 has only a minor influence on the corresponding states.

Of special interest is the dispersion of the singlet band

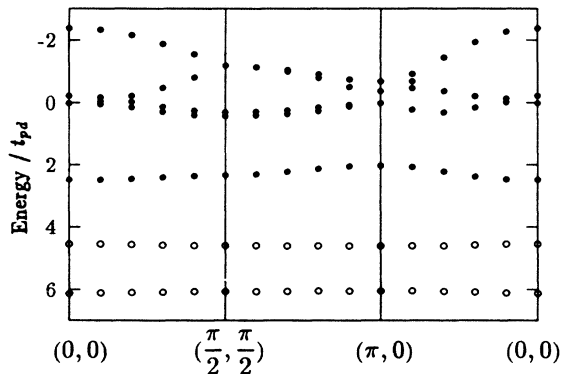


FIG. 10. Dispersion of dominating peaks in the oxygen spectrum (black dots) and inverse oxygen spectrum (circles) at half-filling ($x=0$). The pole positions are shown within the antiferromagnetic Brillouin zone. ($t_{pp} = 0.6$, $\Delta = 4$).

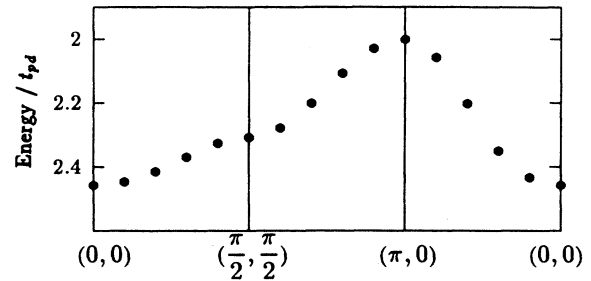


FIG. 11. Dispersion of the singlet pole in the photoemission spectra at half-filling ($x=0$) for the parameter values $t_{pp} = 0.6$, $\Delta = 4$. The \mathbf{k} points at the horizontal axis refer to the antiferromagnetic Brillouin zone.

since it contains the states at the Fermi energy in case of hole doping. Figure 11 is an enlargement of Fig. 10 in the energy range from $\omega = 1.9$ to $\omega = 2.6$. In spite of the large value of $t_{pp} = 0.6$, the singlet bandwidth $W_s = 0.5$ remains rather small. The band maximum is at the Γ point $(0,0)$. For $t_{pp} = 0$, $\Delta = 3$ the singlet bandwidth $W_s = 0.2$ is even smaller as Fig. 12 shows. The bandwidth and the form of the dispersion agree very well with exact diagonalization results for a single hole in the t - J model.¹⁹ Apparently, t_{pp} and the indirect O-O hopping processes proportional to t_{pd}^2/Δ have a counteracting influence on the singlet dispersion. By comparing Fig. 11 with Fig. 12 one realizes that the effective propagation lowers the energy at $(0,0)$ as against the one at $(\frac{\pi}{2}, \frac{\pi}{2})$ or $(\pi, 0)$, whereas t_{pp} has the opposite effect. For that reason, the singlet bandwidth remains small for $t_{pp} = 0.6$.

Since the introduction of the Emery model a large amount of work has been devoted to its electronic excitation spectra in case of half-filling and low levels of doping. A number of authors applied the slave-boson method to it. At half-filling, they also find an energy gap between the photoemission and the inverse photoemission spectra in a parameter range which seems to be reasonable for high-temperature superconductors like $\text{La}_{2-x}\text{Sr}_x\text{CuO}_4$.²⁰⁻²⁴ As a consequence of hole doping, new states appear in the energy gap, which turn the insulator into a metal. These states are in the vicinity of the Fermi level and form a flat band. They corre-

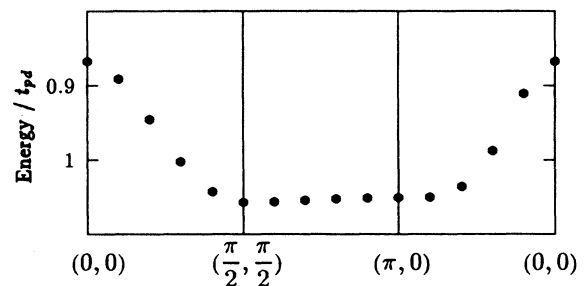


FIG. 12. Dispersion of the singlet pole in the photoemission spectra at half-filling ($x=0$) for the parameter values $t_{pp} = 0$, $\Delta = 3$.

spond to the Abrikosov-Suhl resonance obtained when the slave-boson method is applied to heavy fermion systems. In spite of some similarities they differ considerably from the singlet states presented in this work. In particular, the resonancelike structure vanishes at half-filling. This property is in contrast to our results and the ones of exact diagonalizations of the CuO_2 cluster where the energy gap extends from the upper Hubbard band to the singlet states. Similar results as in slave-boson calculations have been presented in Ref. 25 applying a self-consistent Green's function technique to the Emery model. Thereby, the same shift of singlet states to lower energies with increasing doping has been found as observed in Figs. 6 and 7.

An equivalent type of singlet and triplet states as in our case arises in the photoemission spectra of Refs. 6 and 26. In Ref. 26, the Emery model has been mapped by canonical transformation to an effective singlet-triplet model. Starting out from the reduced Hamiltonian the authors calculated the photoemission and inverse photoemission spectra at half-filling for a paramagnetic ground state. The resulting photoemission spectrum shows roughly the same form as in Fig. 4. As mentioned before the projection method has previously been applied to calculate the photoemission spectrum of oxygen holes for the half-filled case. The results obtained here for $x = 0$ are similar to the previous ones. The distribution of spectral weight in Figs. 4 and 5, however, differs due to the inclusion of direct and indirect O-O hopping in the ground state of H_0 thereby improving the agreement with exact diagonalization results.

The effects of strong correlations on the photoemission and inverse photoemission spectra of the Emery model which have been discussed here are in agreement with experimental results for high-temperature superconductors. O 1s absorption edge measurements of $\text{La}_{2-x}\text{Sr}_x\text{CuO}_{4+\delta}$ for different doping concentrations $0 \leq x \leq 0.3$ (Refs. 27 and 28) reveal the same form of the inverse photoemission spectra as in Fig. 9. At half-filling ($x = 0$), the energy gap is limited by the upper Hubbard band. When the system is doped with holes ($x > 0$), new states appear at the Fermi energy. With increasing doping, additional spectral weight is shifted to these states from the upper Hubbard band. Simultaneously the distance between the two peaks in the absorption spectrum is growing with doping. Although, quantitatively, the experimental decrease in intensity of the upper Hubbard band exceeds our theoretical results and the shift of the peak positions is weaker as in Fig. 9, the qualitative behavior coincides in both cases.

In photoemission experiments on $\text{Bi}_2\text{Sr}_2\text{CaCu}_2\text{O}_8$ (Ref. 29) a flat band is observed which crosses the Fermi energy. Its part below ϵ_F has only a width of 0.2 eV and is much smaller than the LDA predictions, which exceed 0.8 eV. However, these experimental findings agree very well with the width of the flat singlet bands of Figs. 11 and 12. On the other hand, looking at their dispersion in greater detail one recognizes also deviations between theory and experimental observations. Because the system is nonmagnetic the measured form of the dispersion curve shows no antiferromagnetic symmetry. Further-

more, there seems to be a more fundamental discrepancy between theory and experiment with respect to the volume of the Fermi sphere. In the Emery model in the limit $U_d \rightarrow \infty$, there is no Fermi surface at half-filling since the system is an insulator. Consequently, only those charge carriers contribute to the Fermi sphere which are introduced by doping. In photoemission experiments on $\text{Bi}_2\text{Sr}_2\text{CaCu}_2\text{O}_8$, however, the measured Fermi surface agrees quite well with LDA calculations, which predict a large volume.

By comparing the photoemission spectra of $\text{YBa}_2\text{Cu}_3\text{O}_y$ for different hole doping in the range $6.3 \leq y \leq 6.9$ (Ref. 30) one observes an increase in spectral weight of the states close to the Fermi energy with growing hole concentration. This behavior is also found in the photoemission spectra of Fig. 8 for the singlet states although the increase in the measured spectra is more pronounced. Furthermore, there is some controversy whether or not these states are already observed at half-filling. Besides the increase of the singlet weight with hole doping there is also experimental evidence for a simultaneous shift of the singlet position to lower energies. The doping dependence of the Fermi level for $\text{Bi}_2\text{Sr}_2\text{Ca}_{1-y}\text{Y}_y\text{Cu}_2\text{O}_{8+\delta}$ has been investigated in Ref. 31 by comparing the positions of deep-lying core levels for different stoichiometries y . The Fermi level for a hole concentration of $x = 0.2$ is 0.2 eV lower in energy than in the case when the chemical potential just enters the top of the valence band. Since the highest valence band is of very small width this observation may be interpreted as a shift of the singlet states to lower energies by 0.2 eV. This value is in good agreement with the aforementioned O 1s absorption spectra but smaller than in Figs. 6 and 7. Furthermore, this shift of singlet states is supported by measurements of the optical conductivity in $\text{La}_{2-x}\text{Sr}_x\text{CuO}_4$ (Ref. 32). As a consequence of hole doping two new structures arise, i.e., the Drude peak as expected for a metal and an additional maximum in the mid-infrared region. With increasing hole concentration the latter moves to lower energies. The mid-infrared peak may be explained by interband transitions of electrons from occupied states below $\omega = 0.5$ in Fig. 5 into empty states of the singlet band. Therefore, its movement to lower energies indicates a shift of the singlet states in the same direction. In conclusion, all many-particle effects mentioned so far are confirmed at least qualitatively by experiments. These findings support the usefulness of the Emery Hamiltonian as a simplified model for the high-temperature superconducting materials.

VIII. SUMMARY

It was demonstrated that the projection method is a powerful tool for studying strongly correlated electrons. The electronic excitation spectra of the Emery model, which have been calculated and presented, are heavily affected by correlations. The copper level is split into an upper and lower Hubbard band and symmetric linear combinations of oxygen orbitals on a plaquette form singlet and triplet states with the central copper spin.

In order to describe these two-particle states correctly in the limit $U_d \rightarrow \infty$ it is essential to treat exactly the exclusion of doubly occupied copper sites. At half-filling there is an energy gap between the flat singlet band and the upper Hubbard band. Hole doping turns the insulator into a metal. New states arise in the inverse photoemission spectra close to the Fermi energy which are also of singlet character. With increasing doping, additional spectral weight is shifted from the outer regions of the spectra to the states in the vicinity of the Fermi energy. This leads to the surprising fact that for small doping rates the total intensity of the singlets in the photoemission spectra increases with hole doping. In the inverse photoemission spectra, the upper Hubbard band loses intensity, which is shifted to the singlet states close to the Fermi energy. The singlet structure moves as a

whole to lower energies when the hole concentration is enlarged whereas the upper Hubbard band shows the opposite trend. As mentioned before, these results are in very good agreement with exact diagonalization studies of small clusters. Since there is also reasonable agreement with the measured photoemission and inverse photoemission experiments one might hope that the Emery model is appropriate to describe the most important features of the electronic excitations in high-temperature superconductors.

ACKNOWLEDGMENTS

The authors would like to acknowledge a number of useful conversations with Professor K. W. Becker, Dr. W. Brenig, Dr. R. Eder, Dr. P. Horsch, and Dr. W. Stephan.

APPENDIX A: COMMUTATION RELATIONS

The projection operators of the photoemission spectra are found by applying repeatedly the Liouville operator \mathcal{L}'_1 to the creation operators of oxygen holes $c_{m\mathbf{k}\uparrow}^\dagger$. In a similar way the projection operators of the inverse photoemission spectra can be determined by starting from the operator $\hat{d}_{A\mathbf{k}\uparrow}$. The arising commutators $\mathcal{L}'_1 \hat{d}_{\alpha\mathbf{k}\uparrow}^\dagger$, $\mathcal{L}'_1 A_5(\mathbf{k})$, $\mathcal{L}'_1 \hat{d}_{\alpha\mathbf{k}\uparrow}$, and $\mathcal{L}'_1 \bar{A}_2''(\mathbf{k})$ are listed below:

$$\mathcal{L}'_1 \hat{d}_{\alpha\mathbf{k}\uparrow}^\dagger = -2t_{pd}\varphi_\alpha \left\{ p_{\alpha\mathbf{k}\uparrow}^\dagger + \frac{1}{\sqrt{N}} \sum_{\mathbf{q}} p_{\alpha\mathbf{q}\downarrow}^\dagger S_{\alpha(\mathbf{k}-\mathbf{q})}^+ - \frac{1}{N} \sum_{\mathbf{q}_1, \mathbf{q}_2} p_{\alpha\mathbf{q}_1\uparrow}^\dagger \hat{d}_{\alpha\mathbf{q}_2\downarrow}^\dagger \hat{d}_{\alpha(\mathbf{q}_1+\mathbf{q}_2-\mathbf{k})\downarrow} \right\}, \quad (\text{A1})$$

$$\mathcal{L}'_1 A_5(\mathbf{k}) = \frac{2t_{pd}}{\sqrt{N}} \sum_{m\mathbf{q}_1} \phi_{m\mathbf{q}_1} \bar{\phi}_{m\mathbf{q}_1} \hat{d}_{A\mathbf{q}_1\downarrow}^\dagger S_{B(\mathbf{k}-\mathbf{q}_1)}^+ - \frac{2t_{pd}}{N} \sum_{\mathbf{q}_1, \mathbf{q}_2} \{ p_{B\mathbf{q}_1\downarrow}^\dagger p_{B\mathbf{q}_2\uparrow}^\dagger \hat{d}_{B(\mathbf{q}_1+\mathbf{q}_2-\mathbf{k})\downarrow} + p_{B\mathbf{q}_1\downarrow}^\dagger p_{B\mathbf{q}_2\downarrow}^\dagger \hat{d}_{B(\mathbf{k}-\mathbf{q}_1+\mathbf{q}_2)\uparrow}^\dagger \}, \quad (\text{A2})$$

$$\mathcal{L}'_1 \hat{d}_{\alpha\mathbf{k}\uparrow} = 2t_{pd}\varphi_\alpha \left\{ p_{\alpha\mathbf{k}\uparrow} + \frac{1}{\sqrt{N}} \sum_{\mathbf{q}} p_{\alpha\mathbf{q}\downarrow} S_{\alpha(\mathbf{k}-\mathbf{q})}^- - \frac{1}{N} \sum_{\mathbf{q}_1, \mathbf{q}_2} p_{\alpha\mathbf{q}_1\uparrow} \hat{d}_{\alpha\mathbf{q}_2\downarrow}^\dagger \hat{d}_{\alpha(\mathbf{k}-\mathbf{q}_1+\mathbf{q}_2)\downarrow} \right\}, \quad (\text{A3})$$

$$\mathcal{L}'_1 \bar{A}_2''(\mathbf{k}) = \frac{2t_{pd}}{\sqrt{N}} \sum_{m\mathbf{q}_1} \phi_{m\mathbf{q}_1} \bar{\phi}_{m\mathbf{q}_1} \hat{d}_{B\mathbf{q}_1\downarrow} S_{A(\mathbf{k}-\mathbf{q}_1)}^- + \frac{2t_{pd}}{N} \sum_{\mathbf{q}_1, \mathbf{q}_2} \{ p_{A\mathbf{q}_1\downarrow} p_{A\mathbf{q}_2\uparrow} \hat{d}_{A(\mathbf{q}_1+\mathbf{q}_2-\mathbf{k})\downarrow}^\dagger - p_{A\mathbf{q}_2\downarrow} p_{A\mathbf{q}_1\downarrow} \hat{d}_{A(\mathbf{k}-\mathbf{q}_1+\mathbf{q}_2)\uparrow}^\dagger \}. \quad (\text{A4})$$

APPENDIX B: MATRICES OF THE PHOTOEMISSION SPECTRA

The photoemission spectra shown in the preceding sections have been calculated with respect to local creation operators for oxygen and copper holes, $p_{1I\uparrow}^\dagger$ and $\hat{d}_{\alpha I\uparrow}^\dagger$. In the following, we give the definitions of the local correlation functions $G_1^p(\omega)$, $G_\alpha^d(\omega)$ as well as their relations to $G_{mn}^p(\mathbf{k}, \omega)$ or $G_\alpha^d(\mathbf{k}, \omega)$, respectively:

$$G_1^p(\omega) = \langle \Omega | p_{1I\uparrow} \left(\frac{1}{\omega - \mathcal{L}} p_{1I\uparrow}^\dagger \right) | \Omega \rangle_c = \frac{1}{N} \sum_{m\mathbf{n}\mathbf{k}} \beta_{m1}(\mathbf{k}) \beta_{n1}^*(\mathbf{k}) G_{mn}^p(\mathbf{k}, \omega), \quad (\text{B1})$$

$$G_\alpha^d(\omega) = \langle \Omega | \hat{d}_{\alpha I\uparrow} \left(\frac{1}{\omega - \mathcal{L}} \hat{d}_{\alpha I\uparrow}^\dagger \right) | \Omega \rangle_c = \frac{1}{N} \sum_{\mathbf{k}} G_\alpha^d(\mathbf{k}, \omega). \quad (\text{B2})$$

The matrix elements of the susceptibility matrix $\chi(\mathbf{k})$, the frequency matrix $F(\mathbf{k})$, and the coupling matrices $c^p(\mathbf{k})$, $c^d(\mathbf{k})$ are listed below. Thereby, we have used the abbreviation $n_{m\mathbf{k}} = \langle c_{m\mathbf{k}\sigma}^\dagger c_{m\mathbf{k}\sigma} \rangle = \Theta[\epsilon_F - \epsilon_{m\mathbf{k}}]$. The function $n_{m\mathbf{k}}$ is the occupation number of the oxygen band state (m, \mathbf{k}) in the ground state of H_0 . The following matrix elements vanish: $\chi_{m5}, \chi_{m7}, \chi_{56}, \chi_{57}, \chi_{67}, F_{7m}, F_{67}, c_{mA}^d$ for $m = 5, \dots, 7$, and c_{mB}^d for $m \neq 5$. The remaining coupling matrix elements take the form

$$c_{mn}^p(\mathbf{k}) = \chi_{mn}(\mathbf{k}), \quad c_{5B}^d(\mathbf{k}, \mathbf{q}_1) = \frac{2t_{pd}}{\sqrt{N}} \sum_m^{\text{unocc}} \frac{\phi_{m\mathbf{q}_1}}{\epsilon_{m\mathbf{q}_1} - \epsilon_d}, \quad \text{and} \quad c_{mA}^d(\mathbf{k}) = 2t_{pd} \frac{\phi_{m\mathbf{k}}^*}{\epsilon_{m\mathbf{k}} - \epsilon_d} (1 - n_{m\mathbf{k}})$$

for $m = 1, \dots, 4$.

$$\chi_{mn}(\mathbf{k}) = \delta_{mn}(1 - n_{m\mathbf{k}}) - 4t_{pd}^2 \frac{\phi_{m\mathbf{k}}^* \phi_{n\mathbf{k}}(1 - n_{m\mathbf{k}})(1 - n_{n\mathbf{k}})}{(\epsilon_{m\mathbf{k}} - \epsilon_d)(\epsilon_{n\mathbf{k}} - \epsilon_d)}, \quad (\text{B3})$$

$$\begin{aligned} \chi_{55}(\mathbf{k}, \mathbf{q}_1, \mathbf{q}_2) &= \frac{1}{N} \sum_n^{\text{unocc}} \chi_{55}(n, \mathbf{q}_1, \mathbf{q}_2) = \frac{4t_{pd}^2}{N} \sum_{mn}^{\text{unocc}} \frac{|\phi_{m\mathbf{q}_1}|^2 |\phi_{n\mathbf{q}_2}|^2}{(\epsilon_{m\mathbf{q}_1} - \epsilon_d)(\epsilon_{n\mathbf{q}_2} - \epsilon_d)} \\ &+ \delta_{\mathbf{q}_1\mathbf{q}_2} \sum_n^{\text{unocc}} \left(|\phi_{n\mathbf{q}_1}|^2 - 4t_{pd}^2 \sum_m^{\text{unocc}} \frac{|\phi_{m\mathbf{q}_1}|^2 |\phi_{n\mathbf{q}_1}|^2}{(\epsilon_{m\mathbf{q}_1} - \epsilon_d)(\epsilon_{n\mathbf{q}_1} - \epsilon_d)} - \frac{4t_{pd}^2}{N} \sum_{m\mathbf{q}_3}^{\text{unocc}} \frac{|\phi_{n\mathbf{q}_1}|^2 |\phi_{m\mathbf{q}_3}|^2}{(\epsilon_{m\mathbf{q}_3} - \epsilon_d)^2} \right), \end{aligned} \quad (\text{B4})$$

$$\chi_{m6}(\mathbf{k}) = -2t_{pd} \bar{\phi}_{m\mathbf{k}} (1 - n_{m\mathbf{k}}) \frac{1}{N} \sum_{n\mathbf{q}_2}^{\text{unocc}} \frac{|\phi_{n\mathbf{q}_2}|^2}{\epsilon_{n\mathbf{q}_2} - \epsilon_d}, \quad (\text{B5})$$

$$\begin{aligned} \chi_{77}(\mathbf{k}) &= \frac{1}{N} \sum_{m\mathbf{q}_1}^{\text{unocc}} |\phi_{m\mathbf{q}_1}|^2 - \frac{4t_{pd}^2}{N} \sum_{m_1\mathbf{q}_1}^{\text{unocc}} \sum_{m_2}^{\text{unocc}} \frac{|\phi_{m_1\mathbf{q}_1}|^2 |\phi_{m_2\mathbf{q}_1}|^2}{(\epsilon_{m_1\mathbf{q}_1} - \epsilon_d)(\epsilon_{m_2\mathbf{q}_1} - \epsilon_d)} \\ &- \frac{8t_{pd}^2}{N^2} \sum_{m\mathbf{q}_1}^{\text{unocc}} \sum_{n\mathbf{q}_2}^{\text{unocc}} \frac{|\phi_{m\mathbf{q}_1}|^2 |\phi_{n\mathbf{q}_2}|^2}{(\epsilon_{m\mathbf{q}_1} - \epsilon_d)^2} + 4t_{pd}^2 \left(\frac{1}{N} \sum_{m\mathbf{q}_1}^{\text{unocc}} \frac{|\phi_{m\mathbf{q}_1}|^2}{\epsilon_{m\mathbf{q}_1} - \epsilon_d} \right)^2, \end{aligned} \quad (\text{B6})$$

$$\begin{aligned} \chi_{66}(\mathbf{k}) &= \frac{1}{N^2} \sum_{m\mathbf{q}_1}^{\text{unocc}} \sum_{n\mathbf{q}_2}^{\text{unocc}} |\phi_{m\mathbf{q}_1}|^2 |\bar{\phi}_{n\mathbf{q}_2}|^2 + 4t_{pd}^2 \left(\frac{1}{N} \sum_{m\mathbf{q}_1}^{\text{unocc}} \frac{|\phi_{m\mathbf{q}_1}|^2}{\epsilon_{m\mathbf{q}_1} - \epsilon_d} \right)^2 \sum_n^{\text{unocc}} |\bar{\phi}_{n\mathbf{k}}|^2 \\ &- \frac{4t_{pd}^2}{N^2} \sum_{m_2\mathbf{q}_2}^{\text{unocc}} \sum_{m_1\mathbf{q}_1}^{\text{unocc}} \sum_{m_3}^{\text{unocc}} \left\{ \frac{|\phi_{m_1\mathbf{q}_1}|^2 |\phi_{m_3\mathbf{q}_1}|^2 |\bar{\phi}_{m_2\mathbf{q}_2}|^2}{(\epsilon_{m_1\mathbf{q}_1} - \epsilon_d)(\epsilon_{m_3\mathbf{q}_1} - \epsilon_d)} + \frac{\bar{\phi}_{m_1\mathbf{q}_1} \phi_{m_1\mathbf{q}_1} \bar{\phi}_{m_3\mathbf{q}_1}^* \phi_{m_3\mathbf{q}_1}^* |\phi_{m_2\mathbf{q}_2}|^2}{(\epsilon_{m_1\mathbf{q}_1} - \epsilon_d)(\epsilon_{m_3\mathbf{q}_1} - \epsilon_d)} \right\} \\ &- \frac{4t_{pd}^2}{N^2} \sum_{m_1\mathbf{q}_1}^{\text{unocc}} \sum_{m_2\mathbf{q}_2}^{\text{unocc}} \sum_{m_3}^{\text{unocc}} \frac{|\bar{\phi}_{m_1\mathbf{q}_1}|^2 |\phi_{m_2\mathbf{q}_2}|^2 |\phi_{m_3(\mathbf{q}_1+\mathbf{q}_2-\mathbf{k})}|^2}{(\epsilon_{m_3(\mathbf{q}_1+\mathbf{q}_2-\mathbf{k})} - \epsilon_d)^2}, \end{aligned} \quad (\text{B7})$$

$$F_{mn}(\mathbf{k}) = \epsilon_{n\mathbf{k}} \chi_{mn}(\mathbf{k}) + 4t_{pd}^2 \left(\frac{\phi_{m\mathbf{k}}^* \phi_{n\mathbf{k}}}{\epsilon_{m\mathbf{k}} - \epsilon_d} - \frac{\phi_{m\mathbf{k}}^* \phi_{n\mathbf{k}}}{\Delta'} \right), \quad (\text{B8})$$

$$F_{m5}(\mathbf{k}, \mathbf{q}_1) = 4t_{pd}^2 \bar{\phi}_{m\mathbf{k}} \frac{1}{\sqrt{N}} \sum_m^{\text{unocc}} \frac{|\phi_{m\mathbf{q}_1}|^2}{\epsilon_{m\mathbf{q}_1} - \epsilon_d}, \quad F_{6m}(\mathbf{k}) = \epsilon_{m\mathbf{k}} \chi_{6m}(\mathbf{k}), \quad (\text{B9})$$

$$\begin{aligned} F_{55}(\mathbf{k}, \mathbf{q}_1, \mathbf{q}_2) &= \sum_n^{\text{unocc}} \epsilon_{n\mathbf{q}_2} \chi_{55}(n, \mathbf{q}_1, \mathbf{q}_2) - \frac{4t_{pd}^2}{N} \sum_m^{\text{unocc}} \sum_n^{\text{unocc}} \frac{|\phi_{m\mathbf{q}_1}|^2 |\phi_{n\mathbf{q}_2}|^2}{\epsilon_{m\mathbf{q}_1} - \epsilon_d} \\ &+ 4t_{pd}^2 \delta_{\mathbf{q}_1\mathbf{q}_2} \sum_m^{\text{unocc}} |\phi_{m\mathbf{q}_1}|^2 \left(\frac{1}{N} \sum_{n\mathbf{q}_3}^{\text{unocc}} \frac{|\phi_{n\mathbf{q}_3}|^2}{\epsilon_{n\mathbf{q}_3} - \epsilon_d} + \frac{1}{\epsilon_{m\mathbf{q}_1} - \epsilon_d} - \frac{1}{\Delta'} \right), \end{aligned} \quad (\text{B10})$$

$$F_{56}(\mathbf{k}, \mathbf{q}_1) = -2t_{pd} \frac{1}{\sqrt{N}} \sum_m^{\text{unocc}} |\phi_{m\mathbf{q}_1}|^2 \cdot \frac{1}{N} \sum_{n\mathbf{q}_2}^{\text{unocc}} |\bar{\phi}_{n\mathbf{q}_2}|^2, \quad (\text{B11})$$

$$F_{57}(\mathbf{k}, \mathbf{q}_1) = 2t_{pd}^2 \frac{1}{\sqrt{N}} \left| 2 \sum_m^{\text{unocc}} \bar{\phi}_{m\mathbf{q}_1} \phi_{m\mathbf{q}_1} \right|^2 \cdot \frac{1}{N} \sum_{n\mathbf{q}_2}^{\text{unocc}} \frac{|\phi_{n\mathbf{k}}|^2}{\epsilon_{n\mathbf{q}_2} - \epsilon_d}, \quad (\text{B12})$$

$$\begin{aligned}
F_{66}(\mathbf{k}) = & \frac{1}{N^2} \sum_{m_1 \mathbf{q}_1}^{\text{unocc}} \sum_{m_2 \mathbf{q}_2}^{\text{unocc}} \left\{ (\epsilon_{m_1 \mathbf{q}_1} + \epsilon_{m_2 \mathbf{q}_2}) |\phi_{m_1 \mathbf{q}_1}|^2 |\bar{\phi}_{m_2 \mathbf{q}_2}|^2 + \frac{4t_{pd}^2 |\phi_{m_1 \mathbf{q}_1}|^2}{\epsilon_{m_1 \mathbf{q}_1} - \epsilon_d} \left(|\bar{\phi}_{m_2 \mathbf{q}_2}|^2 - |\phi_{m_2 \mathbf{q}_2}|^2 \sum_{m_3}^{\text{unocc}} |\bar{\phi}_{m_3 \mathbf{k}}|^2 \right) \right\} \\
& - \frac{4t_{pd}^2}{N^2} \sum_{m_1 \mathbf{q}_1}^{\text{unocc}} \sum_{m_2 \mathbf{q}_2}^{\text{unocc}} \sum_{m_3}^{\text{unocc}} \left\{ \frac{(\epsilon_{m_1 \mathbf{q}_1} + \epsilon_{m_2 \mathbf{q}_2}) \{ |\phi_{m_1 \mathbf{q}_1}|^2 |\phi_{m_3 \mathbf{q}_1}|^2 |\bar{\phi}_{m_2 \mathbf{q}_2}|^2 + \bar{\phi}_{m_1 \mathbf{q}_1} \phi_{m_1 \mathbf{q}_1} \bar{\phi}_{m_3 \mathbf{q}_1}^* \phi_{m_3 \mathbf{q}_1}^* |\phi_{m_2 \mathbf{q}_2}|^2 \}}{(\epsilon_{m_1 \mathbf{q}_1} - \epsilon_d)(\epsilon_{m_3 \mathbf{q}_1} - \epsilon_d)} \right. \\
& \quad + \frac{(\epsilon_{m_1 \mathbf{q}_1} + \epsilon_{m_2 \mathbf{q}_2}) |\bar{\phi}_{m_1 \mathbf{q}_1}|^2 |\phi_{m_2 \mathbf{q}_2}|^2 |\phi_{m_3(\mathbf{q}_1 + \mathbf{q}_2 - \mathbf{k})}|^2}{(\epsilon_{m_3(\mathbf{q}_1 + \mathbf{q}_2 - \mathbf{k})} - \epsilon_d)^2} \\
& \quad \left. - \frac{(\epsilon_{m_1 \mathbf{q}_1} + \epsilon_{m_3 \mathbf{k}}) |\phi_{m_1 \mathbf{q}_1}|^2 |\bar{\phi}_{m_3 \mathbf{k}}|^2 |\phi_{m_2 \mathbf{q}_2}|^2}{(\epsilon_{m_1 \mathbf{q}_1} - \epsilon_d)(\epsilon_{m_2 \mathbf{q}_2} - \epsilon_d)} \right\} \\
& + \frac{4t_{pd}^2}{N^2} \sum_{m_1 \mathbf{q}_1}^{\text{unocc}} \sum_{m_3}^{\text{unocc}} \sum_{m_2 \mathbf{q}_2}^{\text{unocc}} \left(\frac{1}{\epsilon_{m_1 \mathbf{q}_1} - \epsilon_d} - \frac{1}{\Delta'} \right) \bar{\phi}_{m_1 \mathbf{q}_1}^* \phi_{m_1 \mathbf{q}_1}^* \bar{\phi}_{m_3 \mathbf{q}_1} \phi_{m_3 \mathbf{q}_1} |\phi_{m_2 \mathbf{q}_2}|^2 \\
& + \frac{4t_{pd}^2}{N^2} \sum_{m_1 \mathbf{q}_1}^{\text{unocc}} \sum_{m_2 \mathbf{q}_2}^{\text{unocc}} \left(\sum_{m_3}^{\text{unocc}} \frac{|\phi_{m_3(\mathbf{k} - \mathbf{q}_1 + \mathbf{q}_2)}|^2}{\epsilon_{m_1 \mathbf{q}_1} - \epsilon_d} - \frac{1}{\Delta'} \right) |\bar{\phi}_{m_1 \mathbf{q}_1}|^2 |\phi_{m_2 \mathbf{q}_2}|^2 - \epsilon_d \chi_{66}(\mathbf{k}), \tag{B13}
\end{aligned}$$

$$\begin{aligned}
F_{77}(\mathbf{k}) = & \frac{1}{N} \sum_{m \mathbf{q}_1}^{\text{unocc}} \epsilon_{m \mathbf{q}_1} |\phi_{m \mathbf{q}_1}|^2 - \frac{4t_{pd}^2}{N} \sum_{m_1 \mathbf{q}_1}^{\text{unocc}} \sum_{m_2}^{\text{unocc}} \frac{\epsilon_{m_1 \mathbf{q}_1} |\phi_{m_1 \mathbf{q}_1}|^2 |\phi_{m_2 \mathbf{q}_1}|^2}{(\epsilon_{m_1 \mathbf{q}_1} - \epsilon_d)(\epsilon_{m_2 \mathbf{q}_1} - \epsilon_d)} \\
& - \frac{8t_{pd}^2}{N} \sum_{m \mathbf{q}_1}^{\text{unocc}} \frac{|\phi_{m \mathbf{q}_1}|^2}{(\epsilon_{m \mathbf{q}_1} - \epsilon_d)^2} \cdot \frac{1}{N} \sum_{n \mathbf{q}_2}^{\text{unocc}} \epsilon_{n \mathbf{q}_2} |\phi_{n \mathbf{q}_2}|^2 + \frac{4t_{pd}^2}{N} \sum_{m \mathbf{q}_1}^{\text{unocc}} \frac{|\phi_{m \mathbf{q}_1}|^2}{\epsilon_{m \mathbf{q}_1} - \epsilon_d} \cdot \frac{1}{N} \sum_{n \mathbf{q}_2}^{\text{unocc}} \frac{\epsilon_{n \mathbf{q}_2} |\phi_{n \mathbf{q}_2}|^2}{\epsilon_{n \mathbf{q}_2} - \epsilon_d} \\
& + \frac{4t_{pd}^2}{N} \sum_{m \mathbf{q}_1}^{\text{unocc}} \left(\frac{|\phi_{m \mathbf{q}_1}|^2}{\epsilon_{m \mathbf{q}_1} - \epsilon_d} - \frac{|\phi_{m \mathbf{q}_1}|^2}{\Delta'} \right) + \frac{4t_{pd}^2}{N^2} \sum_{m \mathbf{q}_1}^{\text{unocc}} \sum_{n \mathbf{q}_2}^{\text{unocc}} \frac{|\phi_{m \mathbf{q}_1}|^2 |\phi_{n \mathbf{q}_2}|^2}{\epsilon_{m \mathbf{q}_1} - \epsilon_d}. \tag{B14}
\end{aligned}$$

APPENDIX C: MATRICES OF THE INVERSE PHOTOEMISSION SPECTRA

The local correlation functions of the inverse photoemission spectra and their connection with $\bar{G}_{mn}^p(\mathbf{k}, \omega)$, $\bar{G}_A^d(\mathbf{k}, \omega)$ are as follows:

$$\bar{G}_1^p(\omega) = \langle \Omega | p_{1I\uparrow}^\dagger \left(\frac{1}{\omega - \mathcal{L}} p_{1I\uparrow} \right)^\bullet | \Omega \rangle_c = \frac{1}{N} \sum_{mn\mathbf{k}} \beta_{m1}^*(\mathbf{k}) \beta_{n1}(\mathbf{k}) \bar{G}_{mn}^p(\mathbf{k}, \omega), \tag{C1}$$

$$\bar{G}_A^d(\omega) = \langle \Omega | \hat{d}_{AI\uparrow}^\dagger \left(\frac{1}{\omega - \mathcal{L}} \hat{d}_{AI\uparrow} \right)^\bullet | \Omega \rangle_c = \frac{1}{N} \sum_{\mathbf{k}} \bar{G}_A^d(\mathbf{k}, \omega). \tag{C2}$$

We already mentioned in the preceding sections that the correlation function corresponding to $\hat{d}_{BI\uparrow}$ vanishes due to our ground-state approximation. The projection operator $\bar{A}_2(\mathbf{k}, \mathbf{q})$ is equal to $\bar{A}_2''(\mathbf{k}, \mathbf{q})$ in case of $\epsilon_{1\mathbf{k}} > \epsilon_F$. For $\epsilon_{1\mathbf{k}} \leq \epsilon_F$ it takes the form $2 - \frac{1}{2} [N_o^{-\frac{1}{2}} \bar{A}_2'(\mathbf{k}) - \bar{A}_2''(\mathbf{k}, \mathbf{q})]$. In the following we will give separately the matrix elements for the operators $\bar{A}_2'(\mathbf{k})$ (index "s") and $\bar{A}_2''(\mathbf{k}, \mathbf{q})$ (index "f"). The frequency and susceptibility matrix elements of $\bar{A}_2(\mathbf{k}, \mathbf{q})$ are simple linear combinations of the underlying expressions for $\bar{A}_2'(\mathbf{k})$, $\bar{A}_2''(\mathbf{k}, \mathbf{q})$ and will not be shown here. We start by listing the vanishing matrix elements: $\bar{\chi}_{31}, \bar{\chi}_{sf}, \bar{\chi}_{1f}, \bar{\chi}_{3s}, \bar{F}_{sf}, \bar{F}_{3s}, \bar{c}_{3m}^p, \bar{c}_{3A}^d$, and for $\epsilon_{1\mathbf{k}} > \epsilon_F$: $\bar{c}_{2m}^p, \bar{c}_{2A}^d$. For the remaining coupling matrix elements we find the following results:

$$\bar{c}_{1m}^p(\mathbf{k}) = -2t_{pd} \frac{\phi_{m\mathbf{k}}}{\epsilon_{m\mathbf{k}} - \epsilon_d} (1 - n_{m\mathbf{k}}), \quad \bar{c}_{1A}^d(\mathbf{k}) = \bar{\chi}_{11}(\mathbf{k}), \quad \bar{c}_{2A}^d(\mathbf{k}, \mathbf{q}_1) = \frac{1}{\sqrt{2N_o}} \bar{\chi}_{s1}(\mathbf{k}) \text{ for } \epsilon_{1\mathbf{k}} \leq \epsilon_F,$$

and

$$\bar{c}_{2m}^p(\mathbf{k}, \mathbf{q}_1) = \frac{1}{\sqrt{2N_o}} \left(\phi_{m\mathbf{k}}^* n_{m\mathbf{k}} + 4t_{pd}^2 \phi_{m\mathbf{k}}^* (1 - n_{m\mathbf{k}}) \sum_n^{\text{unocc}} \frac{|\phi_{n\mathbf{k}}|^2}{\epsilon_{n\mathbf{k}} - \epsilon_d} \right) \text{ for } \epsilon_{1\mathbf{k}} \leq \epsilon_F,$$

$$\bar{\chi}_{11}(\mathbf{k}) = 1 - 4t_{pd}^2 \sum_m^{\text{unocc}} \frac{|\phi_{m\mathbf{k}}|^2}{(\epsilon_{m\mathbf{k}} - \epsilon_d)^2}, \tag{C3}$$

$$\bar{\chi}_{s1}(\mathbf{k}) = -2t_{pd} \sum_m^{\text{unocc}} \frac{|\phi_{m\mathbf{k}}|^2}{\epsilon_{m\mathbf{k}} - \epsilon_d}, \quad \bar{\chi}_{33}(\mathbf{k}) = 1, \tag{C4}$$

$$\bar{\chi}_{ss}(\mathbf{k}) = \sum_m^{\text{occ}} |\phi_{m\mathbf{k}}|^2 + 4t_{pd}^2 \left(\sum_m^{\text{unocc}} \frac{|\phi_{m\mathbf{k}}|^2}{\epsilon_{m\mathbf{k}} - \epsilon_d} \right)^2, \quad (\text{C5})$$

$$\bar{\chi}_{3f}(\mathbf{k}, \mathbf{q}_1) = \frac{4t_{pd}}{\sqrt{N}} \sum_m^{\text{unocc}} \sum_n \frac{\phi_{m\mathbf{q}_1} \bar{\phi}_{m\mathbf{q}_1} \phi_{n\mathbf{q}_1}^* \bar{\phi}_{n\mathbf{q}_1}^*}{\epsilon_{m\mathbf{q}_1} - \epsilon_d}, \quad (\text{C6})$$

$$\bar{\chi}_{ff}(\mathbf{k}, \mathbf{q}_1, \mathbf{q}_2) = \delta_{\mathbf{q}_1\mathbf{q}_2} \left[\sum_m^{\text{occ}} |\bar{\phi}_{m\mathbf{q}_1}|^2 \left(1 - \frac{4t_{pd}^2}{N} \sum_{n\mathbf{q}}^{\text{unocc}} \frac{|\phi_{n\mathbf{q}}|^2}{(\epsilon_{n\mathbf{q}} - \epsilon_d)^2} \right) + 4t_{pd}^2 \left| \sum_m^{\text{unocc}} \frac{\bar{\phi}_{m\mathbf{q}_1} \phi_{m\mathbf{q}_1}}{\epsilon_{m\mathbf{q}_1} - \epsilon_d} \right|^2 \right], \quad (\text{C7})$$

$$\bar{F}_{11}(\mathbf{k}) = -\epsilon_d \bar{\chi}_{11}(\mathbf{k}), \quad \bar{F}_{31}(\mathbf{k}) = -\frac{8t_{pd}^2}{N} \sum_{m\mathbf{q}_1}^{\text{unocc}} \sum_n \frac{\phi_{m\mathbf{q}_1} \bar{\phi}_{m\mathbf{q}_1} \phi_{n\mathbf{q}_1}^* \bar{\phi}_{n\mathbf{q}_1}^*}{\epsilon_{m\mathbf{q}_1} - \epsilon_d}, \quad (\text{C8})$$

$$\bar{F}_{s1}(\mathbf{k}) = -2t_{pd} + 2t_{pd} \sum_m^{\text{unocc}} \frac{\epsilon_{m\mathbf{k}} |\phi_{m\mathbf{k}}|^2}{\epsilon_{m\mathbf{k}} - \epsilon_d}, \quad \bar{F}_{1f}(\mathbf{k}, \mathbf{q}_1) = -\frac{2t_{pd}}{\sqrt{N}} \sum_m^{\text{occ}} |\bar{\phi}_{m\mathbf{q}_1}|^2, \quad (\text{C9})$$

$$\bar{F}_{33}(\mathbf{k}) = \frac{4t_{pd}^2}{N} \sum_{m\mathbf{q}_1}^{\text{unocc}} \frac{|\phi_{m\mathbf{q}_1}|^2}{\epsilon_{m\mathbf{q}_1} - \epsilon_d} \left(1 + 2 \sum_n \bar{\phi}_{n\mathbf{q}_1} \phi_{n\mathbf{q}_1} \right) - \epsilon_d \bar{\chi}_{33}(\mathbf{k}), \quad (\text{C10})$$

$$\bar{F}_{ss}(\mathbf{k}) = -\sum_m^{\text{occ}} \epsilon_{m\mathbf{k}} |\phi_{m\mathbf{k}}|^2 - 4t_{pd}^2 \sum_{mn}^{\text{unocc}} \frac{\epsilon_{m\mathbf{k}} |\phi_{m\mathbf{k}}|^2 |\phi_{n\mathbf{k}}|^2}{(\epsilon_{m\mathbf{k}} - \epsilon_d)(\epsilon_{n\mathbf{k}} - \epsilon_d)} + 4t_{pd}^2 \sum_m^{\text{unocc}} \frac{|\phi_{m\mathbf{k}}|^2}{\epsilon_{m\mathbf{k}} - \epsilon_d} + \frac{4t_{pd}^2}{\Delta'} \sum_m^{\text{occ}} |\phi_{m\mathbf{k}}|^2, \quad (\text{C11})$$

$$\begin{aligned} \bar{F}_{ff}(\mathbf{k}, \mathbf{q}_1, \mathbf{q}_2) = \delta_{\mathbf{q}_1\mathbf{q}_2} \left[-\sum_m^{\text{occ}} \epsilon_{m\mathbf{q}_1} |\bar{\phi}_{m\mathbf{q}_1}|^2 \left(1 - \frac{4t_{pd}^2}{N} \sum_{n\mathbf{q}}^{\text{unocc}} \frac{|\phi_{n\mathbf{q}}|^2}{(\epsilon_{n\mathbf{q}} - \epsilon_d)^2} \right) - 4t_{pd}^2 \sum_{mn}^{\text{unocc}} \frac{\epsilon_{m\mathbf{q}_1} \bar{\phi}_{m\mathbf{q}_1} \phi_{m\mathbf{q}_1} \bar{\phi}_{n\mathbf{q}_1}^* \phi_{n\mathbf{q}_1}^*}{(\epsilon_{m\mathbf{q}_1} - \epsilon_d)(\epsilon_{n\mathbf{q}_1} - \epsilon_d)} \right. \\ \left. + \frac{4t_{pd}^2}{N} \sum_m^{\text{occ}} |\bar{\phi}_{m\mathbf{q}_1}|^2 \sum_{n\mathbf{q}}^{\text{unocc}} \frac{|\phi_{n\mathbf{q}}|^2}{\epsilon_{n\mathbf{q}} - \epsilon_d} + \frac{4t_{pd}^2}{\Delta'} \left| \sum_m^{\text{unocc}} \bar{\phi}_{m\mathbf{q}_1} \phi_{m\mathbf{q}_1} \right|^2 \right], \quad (\text{C12}) \end{aligned}$$

$$\bar{F}_{3f}(\mathbf{k}, \mathbf{q}_1) = -\frac{4t_{pd}}{\sqrt{N}} \sum_m^{\text{unocc}} \sum_n \frac{\epsilon_{m\mathbf{q}_1} \phi_{m\mathbf{q}_1} \bar{\phi}_{m\mathbf{q}_1} \phi_{n\mathbf{q}_1}^* \bar{\phi}_{n\mathbf{q}_1}^*}{\epsilon_{m\mathbf{q}_1} - \epsilon_d} + 4t_{pd} \left| \sum_m^{\text{unocc}} \bar{\phi}_{m\mathbf{q}_1} \phi_{m\mathbf{q}_1} \right|^2. \quad (\text{C13})$$

- ¹K. W. Becker and P. Fulde, Z. Phys. B **72**, 423 (1988).
²K. W. Becker and W. Brenig, Z. Phys. B **79**, 195 (1990).
³V. J. Emery, Phys. Rev. Lett. **58**, 2794 (1987).
⁴P. Horsch and W. Stephan, *Proceedings of the NATO Advanced Research Workshop on Interacting Electrons in Reduced Dimensions*, edited by D. Baeriswyl and D. Campbell (Plenum, New York, 1989).
⁵P. Horsch and W. Stephan, *Proceedings of the NATO Advanced Research Workshop on "Dynamics of Magnetic Fluctuations in High Temperature Superconductors"*, edited by G. Reiter, P. Horsch, and G. Psaltakis (Plenum, New York, 1990).
⁶K. W. Becker, W. Brenig, and P. Fulde, Z. Phys. B **81**, 165 (1990).
⁷H. Eskes and G. A. Sawatzky, Phys. Rev. B **43**, 119 (1991).
⁸M. S. Hybertsen, M. Schlüter, and N. E. Christensen, Phys. Rev. B **39**, 9028 (1989).
⁹R. Kubo, J. Phys. Soc. Jpn. **17**, 1100 (1962).
¹⁰R. Zwanzig, *Lectures in Theoretical Physics* (Interscience, New York, 1961), Vol. 3.
¹¹H. Mori, Prog. Theor. Phys. (Kyoto) **34**, 423 (1965).
¹²F. Forster, *Hydrodynamic Fluctuations, Broken Symmetry and Correlation Functions* (Benjamin, New York, 1975).
¹³J. Rossat-Mignod, L. P. Regnault, C. Vettier, P. Burlet, J. Y. Henry, and G. Lapertot, Physica B **169**, 58 (1991).
¹⁴J. Zaanen and A. Oleś, Phys. Rev. B **37**, 9423 (1989).
¹⁵F. C. Zhang and T. M. Rice, Phys. Rev. B **37**, 3759 (1987).
¹⁶T. Tohyama and S. Maekawa, Physica C **191**, 193 (1992).
¹⁷H. J. Schmidt and Y. Kuramoto, Phys. Rev. B **42**, 2562 (1990).
¹⁸H. Eskes, M. B. Meinders, and G. A. Sawatzky, Phys. Rev. Lett. **67**, 1035 (1991).
¹⁹K. J. von Szczepanski, P. Horsch, W. Stephan, and M. Ziegler, Phys. Rev. B **41**, 2017 (1990).
²⁰C. A. Balseiro, M. Avignon, A. G. Rojo, and B. Alascio, Phys. Rev. Lett. **62**, 2624 (1988).
²¹G. Kotliar, P. A. Lee, and N. Read, Physica C **153-155**, 538 (1988).
²²C. A. R. Sá de Melo and S. Doniach, Phys. Rev. B **41**, 6633 (1990).
²³P. C. Pattnaik and D. M. Newns, Phys. Rev. B **41**, 880 (1990).
²⁴J. Brinkmann and N. Grewe, Z. Phys. B **84**, 179 (1991).
²⁵H. Matsumoto, M. Sasaki, and M. Tachiki, Solid State Commun. **71**, 829 (1989).
²⁶R. Hayn, V. Yushankhai, and S. Lovtsov, Phys. Rev. B **47**, 5253 (1993).
²⁷H. Romberg, M. Alexander, N. Nücker, P. Adelman, and J. Fink, Phys. Rev. B **42**, 8768 (1990).
²⁸C. T. Chen, F. Sette, Y. Ma, M. S. Hybertsen, E. B. Stechel,

- W. M. C. Foulkes, M. Schlüter, S-W. Cheong, A. S. Cooper, L. W. Rupp, Jr., B. Batlogg, Y. L. Soo, Z. H. Ming, A. Krol, and Y. H. Kao, *Phys. Rev. Lett.* **66**, 104 (1991).
- ²⁹J. Fink, N. Nücker, H. Romberg, M. Alexander, P. Adelman, R. Claessen, G. Mante, T. Buslaps, S. Harm, R. Manzke, and M. Skibowski, in *Highlights in Condensed Matter Physics and Future Prospects*, edited by L. Esaki (Plenum, New York, 1991).
- ³⁰B. W. Veal, J. Z. Liu, A. P. Paulikas, K. Vandervoort, H. Claus, J. C. Campuzano, C. Olson, A.-B. Yang, R. Liu, C. Gu, R. S. List, A. J. Arko, R. Bartlett, *Physica C* **158**, 276 (1989).
- ³¹M. A. van Veenendaal, R. Schlatmann, G. A. Sawatzky, and W. A. Groen, *Phys. Rev. B* **47**, 446 (1993).
- ³²M. Suzuki, *Phys. Rev. B* **39**, 2312 (1989).